Self-mixing in microtubule-kinesin active fluid from nonuniform to uniform distribution of activity

Teagan E. Bate[1], Megan E. Varney[2], Ezra H. Taylor[1], Joshua H. Dickie[1], Chih-Che Chueh [3], Michael M. Norton [4] & Kun-Ta Wu [1,5,6] ✉

Active fluids have applications in micromixing, but little is known about the mixing kinematics of systems with spatiotemporally-varying activity. To investigate, UV-activated caged ATP is used to activate controlled regions of microtubule-kinesin active fluid and the mixing process is observed with fluorescent tracers and molecular dyes. At low Péclet numbers (diffusive transport), the active-inactive interface progresses toward the inactive area in a diffusion-like manner that is described by a simple model combining diffusion with Michaelis-Menten kinetics. At high Péclet numbers (convective transport), the active-inactive interface progresses in a superdiffusion-like manner that is qualitatively captured by an active-fluid hydrodynamic model coupled to ATP transport. Results show that active fluid mixing involves complex coupling between distribution of active stress and active transport of ATP and reduces mixing time for suspended components with decreased impact of initial component distribution. This work will inform application of active fluids to promote micromixing in microfluidic devices.

Miniaturization enhances production efficiency in chemical engineering, biological engineering, and pharmaceutical manufacturing[1]. For example, microreactors—millimeter-scale devices with channels to mix chemicals and induce chemical reactions—are used to synthesize materials[2], test enzymes[3], and analyze protein conformations[4]. These devices require mixing to homogenize reactants, which is challenging because fluid dynamics at the micron scale are dominated by laminar flow. Mixing at a macroscopic scale is achieved by turbulence-induced advection repeatedly stretching and folding components until a uniform state is reached[5], but at a microscopic scale, turbulence is inhibited (Reynolds number ≪1) and mixing is dominated by molecular diffusion, which is slow and difficult to control. Approaches such as serpentine design[6] and vibrating bubbles[7] have been developed to enhance micromixing, but these are driven by external energy sources and thus require external components that limit miniaturization[1,8].

Active fluids—fluids with microscopic constituents that consume local fuel to generate movement[9–18]—have the potential to enhance mixing at the micron scale. Active fluids self-organize into chaotic turbulence-like flows[19–23] that promote micromixing by repeatedly stretching and folding fluid, even at low Reynolds numbers[24]. Prior work on active mixing has focused on active systems with uniform activity distribution[24–26]. However, mixing processes often start from a state of nonuniformity. Nonuniform distributions of activity in active fluid systems can cause complex dynamics[27–34]. Spatiotemporal patterns of activity that are prescribed from an external source[31,32] or emerge as an additional dynamical variable that coevolves with the system[27–29] have been studied. However, the effect of nonuniform distributions of activity on mixing has not been elucidated.

Here, we study the mixing dynamics of a microtubule-kinesin suspension whose activity is governed by the transport of ATP, the

[1]Department of Physics, Worcester Polytechnic Institute, Worcester, MA 01609, USA. [2]Department of Physics, New York University, New York, NY 10003, USA. [3]Department of Aeronautics and Astronautics, National Cheng Kung University, Tainan 701, Taiwan. [4]School of Physics and Astronomy, Rochester Institute of Technology, Rochester, NY 14623, USA. [5]Department of Mechanical Engineering, Worcester Polytechnic Institute, Worcester, MA 01609, USA. [6]The Martin Fisher School of Physics, Brandeis University, Waltham, MA 02454, USA. ✉e-mail: kwu@wpi.edu

system's energy source. We control the initial distribution of ATP by using caged ATP that can only fuel the fluid after exposure to ultraviolet (UV) light. This allows us to repeatedly observe the transient dynamics that carry the system from heterogeneous activity to homogeneous activity. We explore mixing dynamics ranging from diffusion-dominated to convection-dominated by varying the ATP concentration, composition of kinesin motors, flow cell geometry, and initial distribution of ATP. We contextualize the results with models at two levels of complexity. A simple model captures the mixing dynamics in a diffusion-limited regime, whereas a more complex model that includes active-fluid hydrodynamics reproduces aspects of observed enhanced transport and activity-dependent progression of the active-inactive interface.

Results

Self-mixing of active and inactive fluids

For the experiments presented herein, we select a 3D microtubule-kinesin active fluid because it enhances micromixing[14,24], has tunable activity[35–40], and has established models describing its flow behaviors[41–44]. In microtubule-kinesin active fluid, microtubules self-assemble by depletion into bundles that extend spontaneously, driving chaotic vortical flows. The extension is driven by kinesin motor

dimers that hydrolyze ATP to walk along pairs of antiparallel microtubules and force them in opposite directions (Fig. 1a)[14]. We augment the microtubule-kinesin system with UV light-activated chemistry that allows us to create distinct patterns of activity. In this light-activated system, the ATP is caged—its terminal phosphate is esterified with a blocking group (Fig. 1b)—such that it cannot be hydrolyzed by kinesin motors until the blocking group is removed by exposure to UV light[45,46]. In this system, the activation of the fluid is irreversible. After the fluid is activated, the action of the kinesin motors causes the microtubule network to become a 3D self-rearranging isotropic active gel consisting of extensile microtubule bundles that buckle and anneal repeatedly until the ATP is exhausted[14]. To quantify the evolution of the activity distribution, we suspend fluorescent tracers in the solvent and monitored the tracer motion to extract the speed distribution of active fluid flows (Fig. 1d). To observe the structure of the active suspension, we label microtubules with Alexa 647 (Fig. 1c).

When the fluid is in its inactive state, before it has been activated by UV light, the kinesin motor dimers are bound to microtubules, creating a quiescent crosslinked microtubule network that behaves like an elastic gel (Fig. 1c, top panel). The inactive gel is essentially isotropic, but after the fluid is loaded into a rectangular flow cell ($20 \times 4 \times 0.1$ mm^3) we observe some alignment of the bundles near
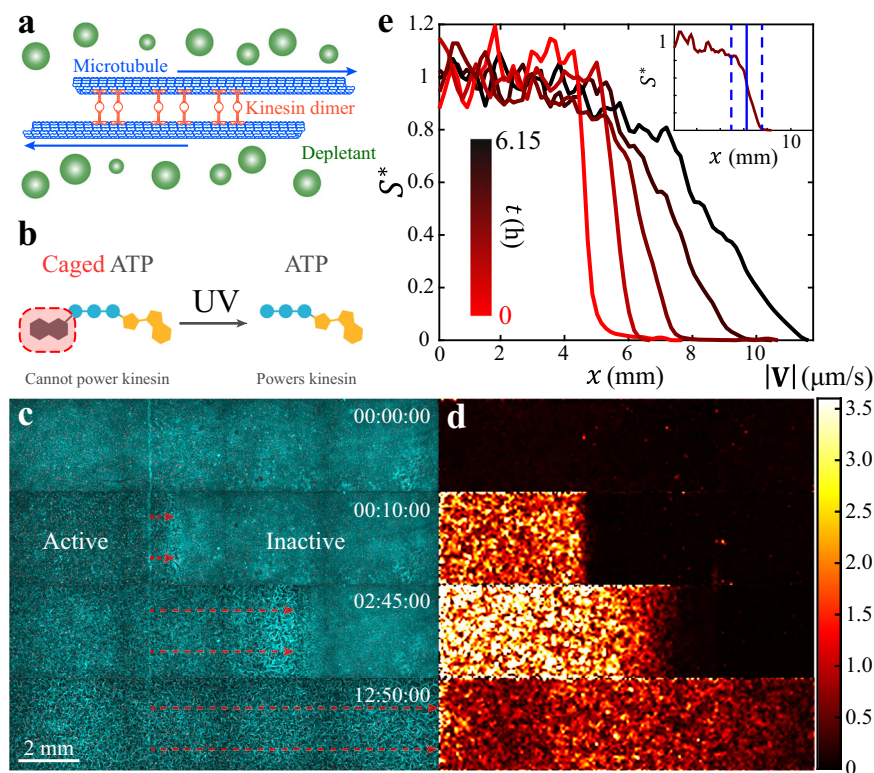

Fig. 1 | (Experimental results) Mixing of activated and inactive microtubule-kinesin fluid. a Microscopic dynamics in microtubule-kinesin active fluid. Depletants force microtubules into bundles where the microtubules can be bridged by kinesin motor dimers. The kinesin motors walk along the microtubules, forcing them to slide apart. The collective sliding dynamics cause the microtubules to form an extensile microtubule network that stirs the surrounding solvents and causes millimeter-scale chaotic flows[14]. **b** To develop an experimental system where we can create a distinct boundary between active and inactive fluid, we synthesize microtubule-kinesin active fluid with caged ATP. The caged ATP is not hydrolysable by kinesin motors, and thus cannot power the active fluid, until it is released by exposure to ultraviolet light[45,46]. This process is not reversible. **c** We expose only one side of the sample to ultraviolet light, which releases the ATP and activates the microtubule-kinesin mixture on that side of the channel. The released ATP

disperses toward the unexposed region, which activates the inactive fluid and expands the active region until the system reaches an activity-homogeneous state (Supplementary Movie 1). Because of the limited speed of multi-position imaging, only one-quarter of the active region is imaged. **d** Tracking tracer particles reveals the speed distribution of fluid flows, showing the activation of the left-hand side by UV light and the expansion of the active region into the inactive region. **e** Binning the same-time speeds vertically across the interface of active and inactive fluids reveals the speed profile S which is normalized as $S^*(x) \equiv [S(x) - s_{in}]/[s_a - s_{in}]$, where s_a is the average of speed profiles in the active zone and s_{in} is the average of speed profiles in the inactive zone. Inset: The interface of the active and inactive fluids is determined as the region where the normalized speed profile is between 0.2 and 0.8 (dashed blue lines). The position of the interface is determined as where the normalized speed profile is 0.5 (solid blue line).
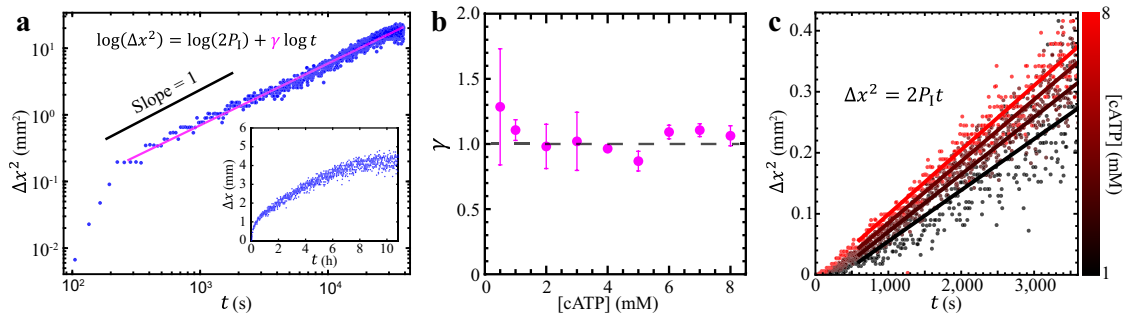
Fig. 2 | (Experimental results) The progression of the active-inactive interface is governed by a diffusion-like process of ATP at the interface. a Squared interface displacement (Δx^2) as a function of time (t) reveals a long-term ($t \gtrsim 200$ s) linear relation: $\Delta x^2 \sim t^\gamma$ with the interface progression exponent $\gamma \approx 1$. Inset: The interface displacement versus time shows that the interface moves rapidly initially and then gradually slows down. **b** The interface progression exponent is $\gamma \approx 1$ on average and is independent of the caged ATP concentration. Each error bar represents the standard deviation of ≥ 3 trials. **c** Selected examples of squared interface displacement versus time for four caged ATP concentrations from 1 mM (black) to 8 mM (red). The progression rate of the interface is characterized with an interface progression coefficient P_I determined by fitting the Δx^2 vs. t data to $\Delta x^2 = 2P_I t$ with P_I as the fitting parameter (colored lines). Increasing caged ATP concentrations increases the interface progression coefficient (steeper fit lines from black to red), which indicates that the interface progresses more quickly at higher caged ATP concentrations.

the boundary (Supplementary Fig. 1)[47]. To create an active-inactive interface, we use a mask to apply UV light to one side of the sample, which releases the ATP and activates the fluid on that side only (Fig. 1c, second panel; Supplementary Movie 1). The spatial pattern of activity evolves from a sharp interface to become increasingly diffuse as the initially active region invades the inactive region (Fig. 1d, second and third panels). We quantify this evolution of activity distribution with the normalized speed profile (Fig. 1e), which shows how the interface between regions widens and shifts as the active and inactive parts of the microtubule system blend over a period of hours.

Characterization of the mixing dynamics

Active fluids enhance the motion of suspended tracers from diffusive (having a mean squared displacement [MSD] proportional to time lapse: MSD $\sim \Delta t^a$ with $a = 1$) to superdiffusive ($a > 1$)[14,26,35]. The progression of the active-inactive interface can also be described as diffusion-like or superdiffusion-like as follows: Suppose the displacement of the active-inactive interface is Δx and the squared interface displacement increases with time as $\Delta x^2 \sim 2P_I t^\gamma$ with the interface progression coefficient P_I and the interface progression exponent γ. If $\gamma = 1$, the progression of the active-inactive interface is defined as diffusion-like; if $\gamma > 1$, the progression of the active-inactive interface is defined as superdiffusion-like.

Because active fluids enhance microscale transport, we hypothesize that the active-inactive interface would progress in a superdiffusion-like manner ($\gamma > 1$). To test this hypothesis, we quantify the displacement of the active-inactive fluid interface as a function of time (Fig. 2a inset) and find that motion of the interface decelerates as the active fluid mixes with the inactive fluid such that the squared interface displacement progresses as $\Delta x^2 \sim t^\gamma$ with an interface progression exponent $\gamma \approx 1$ (Fig. 2a). We repeat the γ measurement for caged ATP concentrations from 0.5 to 8 mM (0.5 mM is enough to maximize the flow speed of active fluid[48]) and consistently find that $\gamma \approx 1$ across this range (Fig. 2b). These results invalidate our hypothesis and suggest that the progression of active-inactive interface is diffusion-like. Notably, while the diffusive time-scaling γ remains consistent, the prefactor P_I exhibits a monotonic but nonlinear dependence on caged ATP concentration (Fig. 2c).

Modeling with Fick's law and Michaelis-Menten kinetics

In the experiments, the interface progression coefficient $\gamma \approx 1$, which suggests that diffusion dominates the dynamics of the active-inactive interface. To contextualize our observations, we construct a minimal model that combines diffusion of ATP with a previously measured relation between ATP concentration and local fluid velocity[48]. Herein, we model ATP's dispersion using Fick's law of diffusion:

$$\frac{\partial C(\mathbf{r}, t)}{\partial t} = D\nabla^2 C(\mathbf{r}, t), \qquad (1)$$

where $C(\mathbf{r}, t)$ represents the spatial distribution of ATP concentrations at time t and D is the diffusion coefficient of ATP in active fluid. We choose $D = 140$ μm²/s, which is one-fifth the diffusion coefficient of ATP in water[49], because the crosslinked microtubule network makes the fluid more viscous than water[50] and our measurement on diffusion coefficient of suspended fluorescein is one-fifth of its reported value in aqueous solution (Supplementary Note 1). To simplify the modeling, we consider a 1D active fluid system confined in a segment, $x = 0 - L$, where $L = 20$ mm is the segment length, and apply no-flux boundary conditions

$$\frac{\partial}{\partial x}C(x=0, t) = \frac{\partial}{\partial x}C(x=L, t) = 0. \qquad (2)$$

To mimic the UV-activation process (Fig. 1c), we initiate the ATP concentration with a step function

$$C(x, t=0) = \frac{C_0}{2}\text{erfc}\left(\frac{x - x_0}{2\sqrt{\epsilon D}}\right), \qquad (3)$$

where $C_0 = 0.5-8$ mM, the initial ATP concentrations in the activated region; erfc is the complementary error function; and $x_0 = 10$ mm is the initial position of the active-inactive interface. We choose $\epsilon = 0.001$ to generate a sharp concentration transition at the interface. We numerically solve Eqs. (1–3) to determine the spatial and temporal distribution of ATP concentrations (Fig. 3a; Supplementary Movie 2). To relate the evolving ATP distribution to local flow speed, we leverage previous experimental results[48] that find the average velocity in bulk samples follows Michaelis-Menten kinetics

$$\bar{v}(x, t) = \bar{v}_m\left[\frac{C(x, t)}{C(x, t) + K}\right], \qquad (4)$$

where $\bar{v}$ is the mean speed of active fluid, $\bar{v}_m = 6.2$ μm/s is the saturated mean speed, and $K = 270$ μM is the ATP concentration that leads to half of the saturated mean speed, $\bar{v}_m/2$. (Model selection is described in Supplementary Note 2). The mean speed distributions
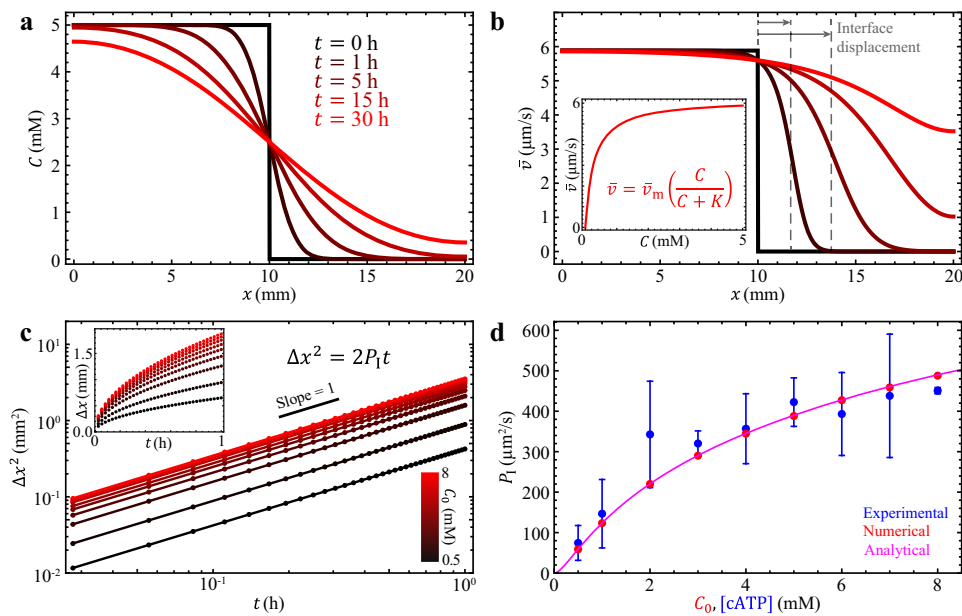
Fig. 3 | (Modeling results) Fick's law of diffusion and Michaelis-Menten kinetics captures the diffusion-like mixing of active and inactive fluids. a The simulated distribution of ATP concentrations starts as a step function (black, $t = 0$ h) and then develops into a smoothed hill function (red, $t = 30$ h) as ATP evolves from a one-sided distribution to a homogeneous state. **b** The model converts the ATP distribution into the speed distribution of active fluid via Michaelis-Menten kinetics: $\bar{v} = \bar{v}_m[C/(C + K)]$, where $\bar{v}_m = 6.2\,\mu$m/s and $K = 270\,\mu$M (based on our previous studies[48]). The corresponding mean speed distribution of active fluid evolves from a step function distribution (black, $t = 0$ h) to a near-constant function (red, $t = 30$ h) (Supplementary Movie 2). Inset: The plot of the Michaelis-Menten equation (Eq. 4). **c** In the simulation, the diffusion-driven mixing process leads the squared interface displacement to be proportional to time, regardless of initial ATP

concentration C_0 (see Supplementary Note 3 for derivation of $\Delta x^2 \propto t$). Inset: Interface displacement increases rapidly with time initially, followed by a gradual deceleration similar to the experimental observation (Fig. 2a inset). **d** In the simulation, the interface progression coefficient P_I is determined by fitting the Δx^2 vs. t data (Panel **c**) to $\Delta x^2 = 2P_I t$ with P_I as fitting parameter. The model P_I increases with the initial concentration of ATP, C_0 (red dots), similarly to how the experimentally analyzed P_I varies with caged ATP concentration (blue dots; each error bar represents the standard deviation of ≥ 3 trials). The model P_I and experimental P_I differ by only ~10%. The magenta curve shows the analytical solution, $P_I(C_0)$ (Supplementary Equation 7), which reproduces the numerical results (red dots). (See Supplementary Note 3 for derivation of P_I as a function of C_0).

(Fig. 3b) show that initially one side of the sample is activated (black) and then the sample evolves toward a more uniformly activated state (red). The squared interface displacement of the active-inactive interface increases linearly with time, $\Delta x^2 \sim t$ (Fig. 3c; see Supplementary Note 3 for derivation of $\Delta x^2 \propto t$), which matches our experimental observation of $\gamma \approx 1$ (Fig. 2a, b). Further, we compare the dependency of the interface progression coefficient P_I (determined by fitting Δx^2 vs. t data to $\Delta x^2 = 2P_I t$ with P_I as the fitting parameter; Figs. 2c and 3c) on initial ATP concentrations between experiment and model and also find excellent agreement (differed by ~10%; Fig. 3d). Taken together, the agreement between simulation and experiment on the scaling of the dynamics (Figs. 2b and 3c) and dependency on initial ATP concentration (Fig. 3d) indicate that the dispersion of ATP is dominated by diffusion and that Michaelis-Menten kinetics are appropriate for a coarse-grained model to connect ATP concentration with local flow speed of active fluid[48], without the need to introduce a more complex hydrodynamic model[42,51].

Superdiffusion-like progression of active-inactive interface
The success of the diffusion-limited model suggests that the active transport in the active fluid systems studied above is dominated by diffusion. This inspires us to question whether the progression of active-inactive interface will become superdiffusion-like when the active transport becomes convection-like[27,28]. To answer this question, we varied experimental parameters to explore a wider range of fluid flow speeds. To achieve lower flow speeds, we alter the composition of motor proteins by replacing a fraction of the processive motors (K401), which exert force on microtubules continuously, with non-processive motors (K365) that detach after each force application. The

reduced number of processive motors has the net effect of driving the extensile motion of microtubules more slowly (Fig. 4a inset left)[36,48]. To achieve higher flow speeds, we increase the height of the sample container to decrease hydrodynamic drag (Fig. 4a inset right)[48,52]. Throughout these experiments, we keep the caged ATP concentration constant (5 mM).

As in the previous experiments, we analyze the spatiotemporal progression of activity to find the interface progression exponent γ as a function of the average flow speed in the bulk of the initially activated area, $\bar{v}_{ab}$ (Fig. 4a). Because changing channel geometry alters the characteristic size of vortices in active fluids[39], we unify our datasets by plotting γ as a function of the Péclet number, Pe (Fig. 4b), defined as Pe $\equiv \bar{v}_{ab}l_c/D$ where l_c is the correlation length of flow velocity (see Supplementary Note 4) and $D = 140\,\mu$m^2/s is our estimate of ATP diffusion in the system (see Supplementary Note 1)[53,54]. The Péclet number is a dimensionless quantity representing the ratio of convective transport rate to diffusive transport rate. A larger Péclet number (typically of order 10 or above) indicates convection-dominated active transport, and a smaller Péclet number (typically of order 1 or below) indicates diffusion-dominated active transport. Our data show that for Pe $\lesssim 3$, the interface progression exponent remains $\gamma \approx 1$ (Fig. 4b), which corresponds to the regime captured by our model (Fig. 3). Then as Pe increases to greater than 3, γ grows monotonically (Fig. 4b). For the largest Pe explored in our experiments (Pe ≈ 16), γ reaches ~1.7, which indicates that convective processes are beginning to emerge and dominate the active transport. Overall, our data suggest that as the active transport transitions from diffusion-dominated (Pe $\lesssim 3$) to convection-dominated (Pe $\gtrsim 3$) regimes, the progression of active-inactive interfaces transitions from diffusion-like ($\gamma \approx 1$) to superdiffusion-like ($\gamma > 1$).
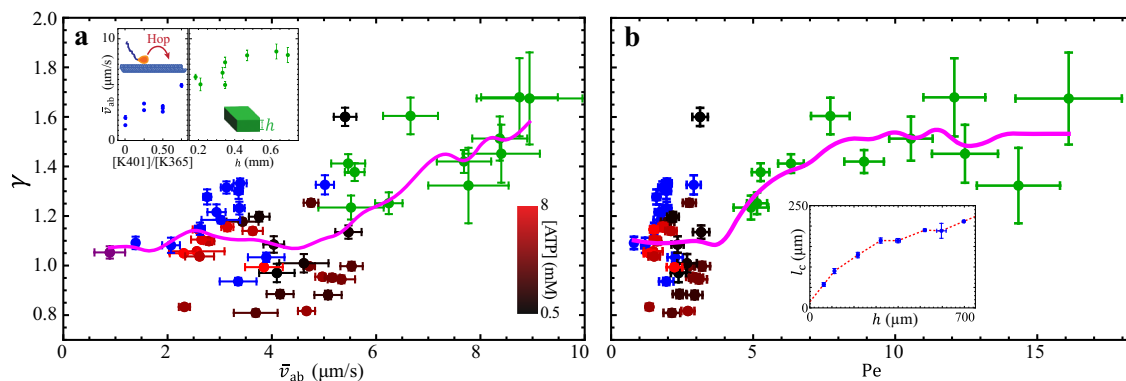
Fig. 4 | (Experimental results) Transition of active-inactive interface progression. Progression of the active-inactive interface transitions from diffusion-like ($\gamma \approx$ 1) to superdiffusion-like ($\gamma > 1$) as the active transport changes from diffusion-dominated (Pe $\lesssim$ 3) to convection-dominated (Pe $\gtrsim$ 3). **a** The active-inactive interface progression exponent (γ) increases with the flow-speed level of the active fluid ($\bar{v}_{ab}$). Shown are data from experiments with low ATP concentration (0.5 mM, black dots), high ATP concentration (8 mM, red dots), decreased flow speeds (from nonprocessive motors partially replacing processive motors; blue dots), increased flow speeds (from increased sample height; green dots)[48], and both nonprocessive motors and increased sample height (purple dot). The magenta curve represents the moving average of γ. Although the analyzed γ from each experiment is noisy, the moving averaged γ exhibits an overall monotonic increase with the flow-speed level of active fluid $\bar{v}_{ab}$. Each dot represents one experimental measurement. Each error bar in γ represents the slope fitting error in $\ln\Delta x^2 = \ln(2P_1) + \gamma\ln t$ (Fig. 2a), and

each error bar in $\bar{v}_{ab}$ represents the standard deviation of flow speeds in the active region. Inset: The flow-speed level of the active fluid is tuned by replacing processive motors (K401) with nonprocessive motors (K365) with the same overall motor concentrations (120 nM) (left)[36,48] or by altering the sample height (right)[48,52]. **b** The same data as in Panel a, plotted as a function of Péclet number, Pe $\equiv \bar{v}_{ab}l_c/D$, where l_c is the correlation length of flow velocity in active fluid deduced from sample container height h (inset) and D is the diffusion coefficient of ATP. Each error bar in γ is the same as in Panel a, and each error bar in Pe represents propagated uncertainties from $\bar{v}_{ab}$ in Panel a and l_c in inset. Inset: Correlation length of flow velocity in active fluid l_c increases monotonically with sample container height h[39]. The red dashed line represents the line interpolation of blue dots. The error bars represent the standard deviations of two trials. (See Supplementary Note 4 for measurements and analyses of l_c).

Dispersion of UV-activated fluorescent dyes

To this point, we have characterized the mixing of active and inactive fluids by the progression of the interface between them; however, like milk blending into coffee, the mixing process often involves dispersion of suspended components. To characterize how suspended components disperse during the progression of the active-inactive interface, we design another series of experiments with suspended components that are initially nonuniform. We dope inactive fluid with suspended UV-activated fluorescent dyes and expose one side of the sample container to UV light, which simultaneously activate the fluid and the fluorescent dye. We find that in an inactive sample ($\bar{v}_{ab} = 0$), where dyes disperse only by molecular diffusion, the dye barely disperse, whereas in a sample where one side is activated ($\bar{v}_{ab} = 8.2\,\mu m/s$), the dyes are transported by active fluid flows and almost completely disperse through the sample in 4 hours (Fig. 5a). To quantify the dispersion rate, we adopt Saintillan and Shelley's method[25] to analyze the normalized multiscale norm of dye brightness as a function of time: $\hat{s}(t) \equiv |s(t)|/|s(0)|$, where

$$|s| \equiv \left[\sum_k \frac{|s_k|^2}{\sqrt{1+l^2k^2}} \right]^{1/2},\quad (5)$$

s_k is the Fourier coefficient at wave vector k in a Fourier expansion of the dye brightness and $l = 4.84\,\mu m$ is the pixel size of the micrographs. We find that the normalized multiscale norm decays faster as $\bar{v}_{ab}$ increases from 0 to 8.2 μm/s (Fig. 5b). In light of reports that the norm decays exponentially[25], we quantify the decay rate by fitting the first hour $\hat{s}(t)$ data to $\ln\hat{s} = -t/t_0$ with t_0 (mixing time) as the fitting parameter (Fig. 5b inset) and find that the mixing time decreases with flow speed of active fluid (Fig. 5c inset). When the fluid is inactive ($\bar{v}_{ab} = 0$), dye dispersion is dominated by molecular diffusion and the mixing time is 24 hours; slightly activating the fluid ($\bar{v}_{ab} = 2\,\mu m/s$) reduces the mixing time to 8 hours, which demonstrates that active fluid flows enhance the mixing process of suspended components[26].

To reveal how the mechanism of active transport (i.e., diffusion-dominated or convection-dominated) alters the mixing time, we analyze the mixing time as a function of the Péclet number and find that the mixing time monotonically decreases as the active transport becomes more convection-like (Fig. 5c). Notably, there is no discernible transition in mixing time as the active transport transitions from diffusion-dominated to convection-dominated, although there is a transition in the progression of active-inactive interfaces (Fig. 4b). This dependence of mixing time on the Péclet number in active-inactive fluid systems is similar to that in an activity-uniform active fluid system (Supplementary Note 5 and Supplementary Fig. 6b), which shows that Péclet number is the controlling parameter for mixing time of suspended components in active fluid systems, regardless of the distribution of activity.

Continuous active fluid model

Our experimental data show that as the active transport becomes more convection-like, the active-inactive interface progression transitions from diffusion-like to superdiffusion-like (Fig. 4b) and the mixing time of suspended components decreases monotonically (Fig. 5c). To determine whether this complex mixing process can be modeled with an existing active fluid model, we adopted Varghese et al.'s model[51] because it successfully describes the transition from coherent to chaotic flow in 3D microtubule-kinesin active fluid systems[52]. The model describes microtubules as self-elongating rods whose nematic order, **Q**, is subject to spontaneous decay due to the rods' rotational molecular diffusion and reorientation by solvent flow. Thus, the dimensionless kinetic equation for **Q** can be written as:

$$\partial_{t^*}\mathbf{Q} + \mathbf{u}\cdot\nabla_*\mathbf{Q} + \mathbf{Q}\cdot\boldsymbol{\Omega}^* - \boldsymbol{\Omega}^*\cdot\mathbf{Q} = -\mathbf{Q} + \nabla_*^2\mathbf{Q} + \lambda\left[\frac{2}{d}\mathbf{E}^* + \mathbf{Q}\cdot\mathbf{E}^* + \mathbf{E}^*\cdot\mathbf{Q} - \frac{2}{d}\mathrm{Tr}\left(\mathbf{Q}\cdot\mathbf{E}^*\right)\mathbf{I}\right],$$

$$(6)$$

where t^* is the dimensionless time, ∇_* is the dimensionless spatial gradient operator, ∇_*^2 is the dimensionless Laplacian operator, $\boldsymbol{\Omega}^* \equiv [(\nabla_*\mathbf{u})^T - \nabla_*\mathbf{u}]/2$ is the dimensionless vorticity tensor,
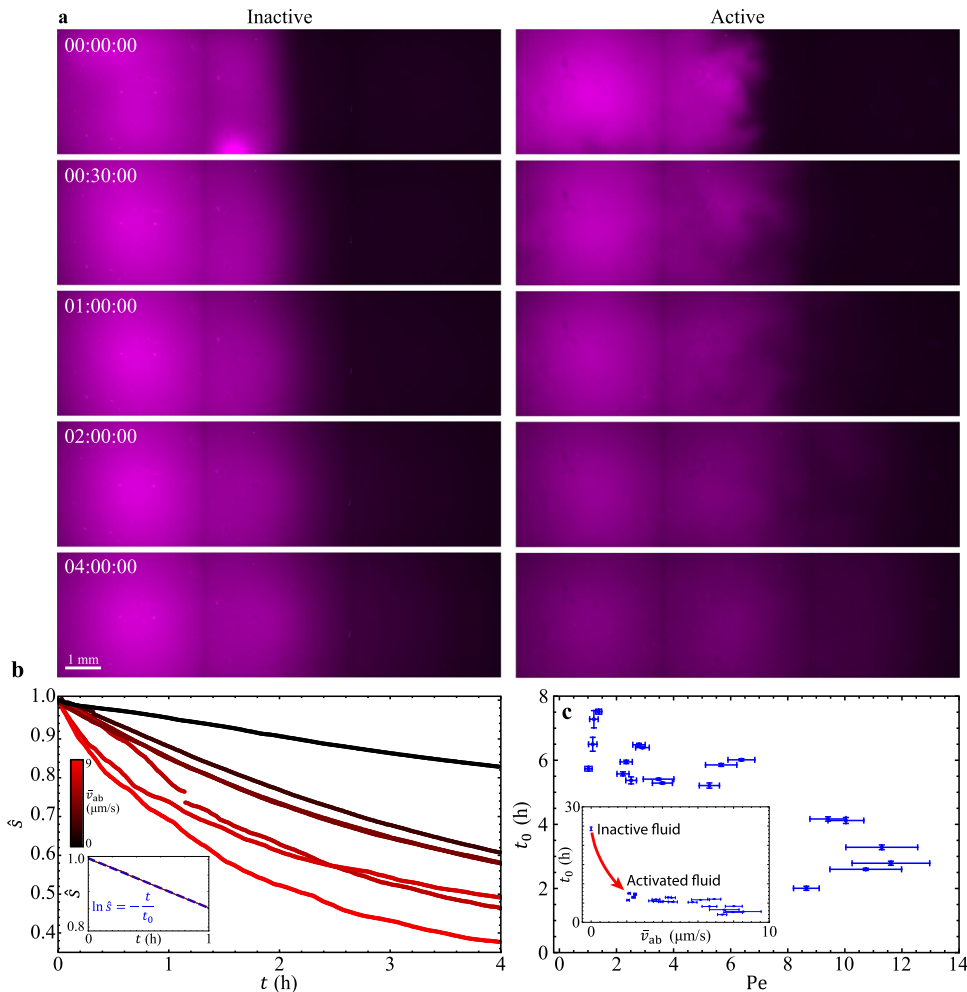
Fig. 5 | (Experimental results) Dispersion of UV-activated fluorescent dyes in active-inactive fluid systems. Active fluid flows promote mixing of UV-activated fluorescent dyes, which are initially activated in the left-hand side of the container only. **a** Dispersion of UV-activated fluorescent dyes (magenta) in inactive ($\bar{v}_{ab}$ = 0; left column) and active ($\bar{v}_{ab}$ = 8.2 μm/s; right column) microtubule-kinesin fluid. Active fluid flows actively transport fluorescent dyes and enhance their dispersion. Time stamps are hour:minute:second. (See also Supplementary Movie 3.) **b** Selected examples of normalized multiscale norm vs. time for different active bulk flow speeds, $\bar{v}_{ab}$. Normalized multiscale norm $\hat{s}(t)$ decreases faster in a faster-flowing active fluid system. Inset: The normalized multiscale norm, $\hat{s}(t)$, in log-linear axes behaves as a straight line, which suggests that the norm decays exponentially with time. The decay time scale t_0 (or mixing time) is determined by fitting the

normalized multiscale norm versus time data to $\ln\hat{s} = -t/t_0$ with t_0 as the fitting parameter (dashed blue line). **c** The mixing time decreases monotonically with Péclet number, which demonstrates that a stronger convection mechanism leads to faster mixing of suspended components. Each dot represents one experimental measurement. Each error bar in t_0 represents the slope fitting error in $\ln\hat{s} = -t/t_0$ (Panel **b** inset), and each error bar in Pe (defined as Pe $\equiv \bar{v}_{ab}l_c/D$) represents propagated uncertainties from $\bar{v}_{ab}$ (see inset) and l_c (see Supplementary Fig. 5d). Inset: Mixing time, t_0, as a function of active bulk mean speed, $\bar{v}_{ab}$. Each error bar in t_0 is the same as in Panel **c**, and each error bar in $\bar{v}_{ab}$ represents the standard deviation of flow speeds in the active region. Notably, the mixing time of the inactive fluid system ($\bar{v}_{ab}$ = 0) is 24 hours (top-left dot); minimally activating the fluid ($\bar{v}_{ab}$ = 2 μm/s) reduces the mixing time to 8 hours.

$\mathbf{E}^* \equiv [(\boldsymbol{\nabla}_*\mathbf{u})^{\mathrm{T}} + \boldsymbol{\nabla}_*\mathbf{u}]/2$ is the dimensionless strain rate tensor, $\lambda = 1$ is the flow alignment coefficient, and d is the system dimensionality. The dimensionless flow field $\mathbf{u}$ is governed by the Stokes equation

$$\nabla_*^2\mathbf{u} - \boldsymbol{\nabla}_*p^* - \boldsymbol{\nabla}_* \cdot \boldsymbol{\sigma}_a = 0 \qquad (7)$$

and incompressibility constraint ($\boldsymbol{\nabla}_* \bullet \mathbf{u} = 0$), where p^* is the dimensionless pressure and $\boldsymbol{\sigma}_a \equiv \alpha^*\mathbf{Q}$ is the dimensionless active stress exerted by self-elongating rods with a dimensionless activity coefficient α^*[55]. Because the activity coefficient increases with ATP concentration[56], we select an α-ATP relation[57]

$$\alpha^* = \alpha_0^* \frac{C}{C+K} , \qquad (8)$$

where α_0^* is the dimensionless activity level, C is the ATP concentration, and K = 270 μM[48]. We select this relation because it captures the

dynamics of microtubule bundle extension and kinesin kinetics (Michaelis-Menten), which play critical roles in the activity of microtubule-kinesin active fluid systems[58,59]. Finally, given that ATP diffuses as a result of thermal fluctuation as well as flows with the active fluid, we model ATP dispersion with a convection-diffusion equation:

$$\partial_{t^*}C = D^*\nabla_*^2C - \mathbf{u} \cdot \boldsymbol{\nabla}_*C, \qquad (9)$$

where D^* is the dimensionless ATP molecular diffusion coefficient. To simplify modeling, we consider a 2D active fluid system ($d = 2$)[51] confined in a 112×22 rectangular boundary with no-slip boundary condition for flows ($\mathbf{u} = \boldsymbol{0}$) and no-flux boundary condition for rods ($\mathbf{n} \cdot \boldsymbol{\nabla}_*\mathbf{Q} = \boldsymbol{0}$, where n represents a unit vector normal to boundaries). To solve the equations for $\mathbf{Q}$, $\mathbf{u}$, and C (Eqs. 6, 7, and 9), we determine the initial conditions as quiescent solvent ($\mathbf{u} = \boldsymbol{0}$) under uniform pressure ($p^* = 0$) with the rods in an isotropic state [$Q_{xx} = -Q_{yy} = 2.5 \times 10^{-4}$ rn(**r**) and $Q_{xy} = Q_{yx} = 5 \times 10^{-4}$rn(**r**), where
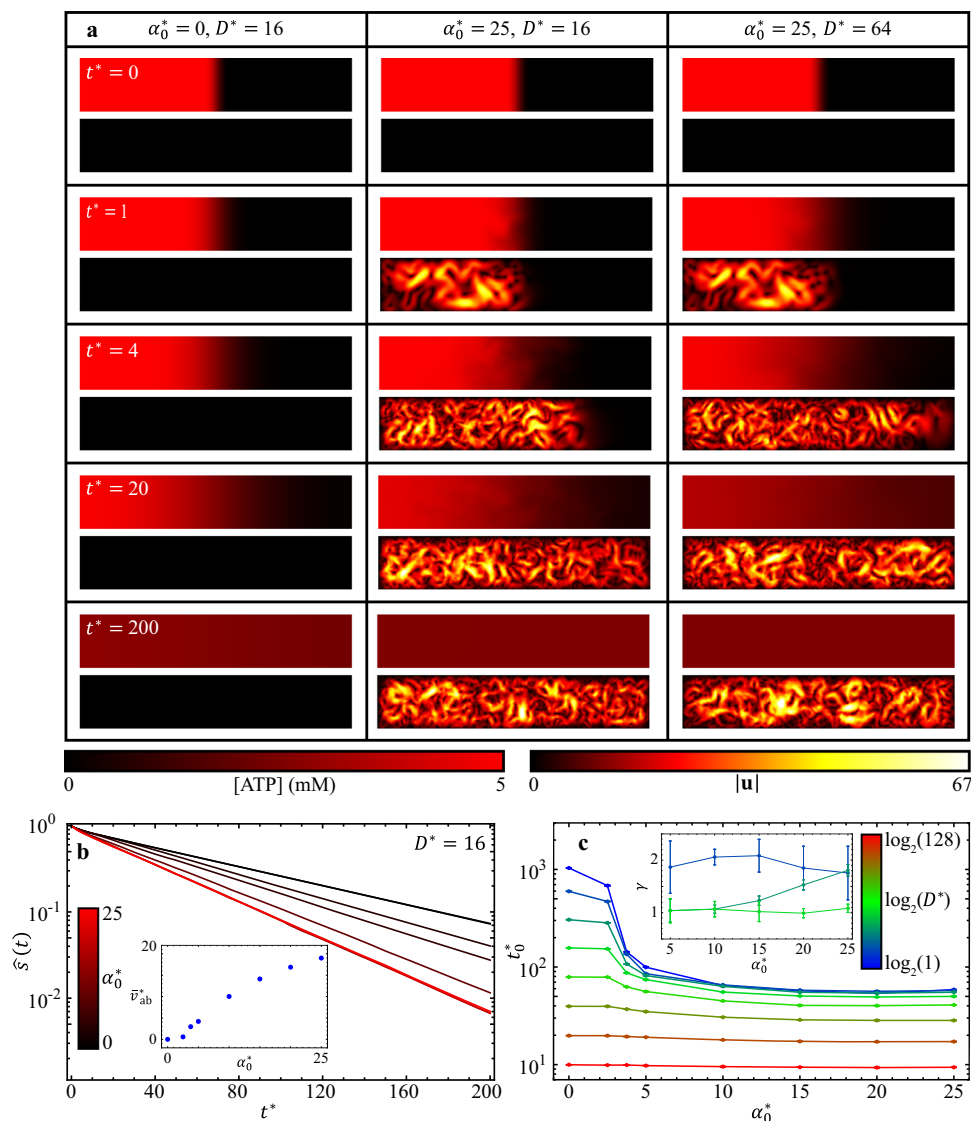
Fig. 6 | (Modeling results) A continuous active fluid simulation reveals that the mixing time of ATP depends on the dimensionless molecular diffusion coefficient of ATP and the dimensionless activity level of active fluid. a Table of ATP concentration (top panels) and active fluid flow speed (bottom panels) maps for various dimensionless activity levels α_0^* and molecular diffusion coefficients D^*. When the fluid has no activity ($\alpha_0^* = 0$; left column), ATP disperses to the right side of the system only by molecular diffusion; the dispersion is enhanced when the active fluid starts to flow and actively transport ATP ($\alpha_0^* = 25$; middle column). The dispersion is further enhanced when ATP diffuses significantly faster ($D^* = 64$; right column) (Supplementary Movie 4). **b** Evolution of normalized multiscale norm for $\alpha_0^* = 0$–25 while keeping $D^* = 16$. The normalized multiscale norms decay

exponentially with time: $\hat{s} = \exp(-t^*/t_0^*)$, where t_0^* is the dimensionless mixing time. Inset: Dimensionless mean speed of active fluid in active region $\bar{v}_{ab}^*$ monotonically increases with dimensionless activity level α_0^*. **c** Dimensionless ATP mixing times, t_0^*, as a function of dimensionless activity level, α_0^*, for various dimensionless molecular diffusion coefficients, D^*. Increasing both α_0^* and D^* decreases mixing time monotonically. Each error bar in t_0^* represents the fitting error of $\hat{s}$ vs. t^* to $\ln\hat{s} = -t^*/t_0^*$ (Panel **b**). Inset: Active-inactive interface progression exponent γ as a function of dimensionless activity level α_0^* for dimensionless molecular diffusion coefficients $D^* = 2$ (dark blue), 4 (dark green), and 8 (light green). Each error bar in γ represents the slope fitting error as in Fig. 2a. Increasing D^* decreases γ (from dark blue to light green curve), whereas increasing α_0^* increases γ (dark green curve).

rn(**r**) is a spatially uniform random number between −1 and +1] and 5 mM of ATP distributed on only one side of the system. Then we evolve the fluid flows and ATP distributions for 200 units of dimensionless time ($t^* = 0$–200) with the finite element method[60].

Our modeling results (Supplementary Movie 4) show that in an inactive system ($\alpha_0^* = 0$; $D^* = 16$; Fig. 6a, left column), ATP disperses only by molecular diffusion, but when one side of the sample is activated ($\alpha_0^* = 25$; $D^* = 16$; middle column), the system develops chaotic turbulence-like mixing flows that actively transport the ATP toward the inactive region. In a third simulation where the ATP molecular diffusion rate is increased ($\alpha_0^* = 25$; $D^* = 64$; right column), the mixing process speeds up. These simulation results show that the process of

ATP dispersion is controlled by both molecular diffusion of ATP and active fluid-induced convection.

To quantify the efficacy of ATP mixing by active fluid, we analyze the normalized multiscale norm of ATP concentrations as a function of time[25] for $\alpha_0^* = 0$–25 and $D^* = 1$–128 (Eq. (5) with $l = 1$). We find that the norms decay exponentially with time: $\hat{s} \sim \exp(-t^*/t_0^*)$, where t_0^* is the dimensionless mixing time (Fig. 6b), which is consistent with results reported by Saintillan and Shelley[25]. We analyze mixing time as a function of dimensionless activity level, α_0^*, for each dimensionless molecular diffusion coefficient D^* (Fig. 6c) and find that when ATP diffuses slowly ($D^* \lesssim 16$; blue to light green curves), mixing time decreases with increasing activity level or faster active transport (Fig. 6b inset), which is consistent with our experimental observation
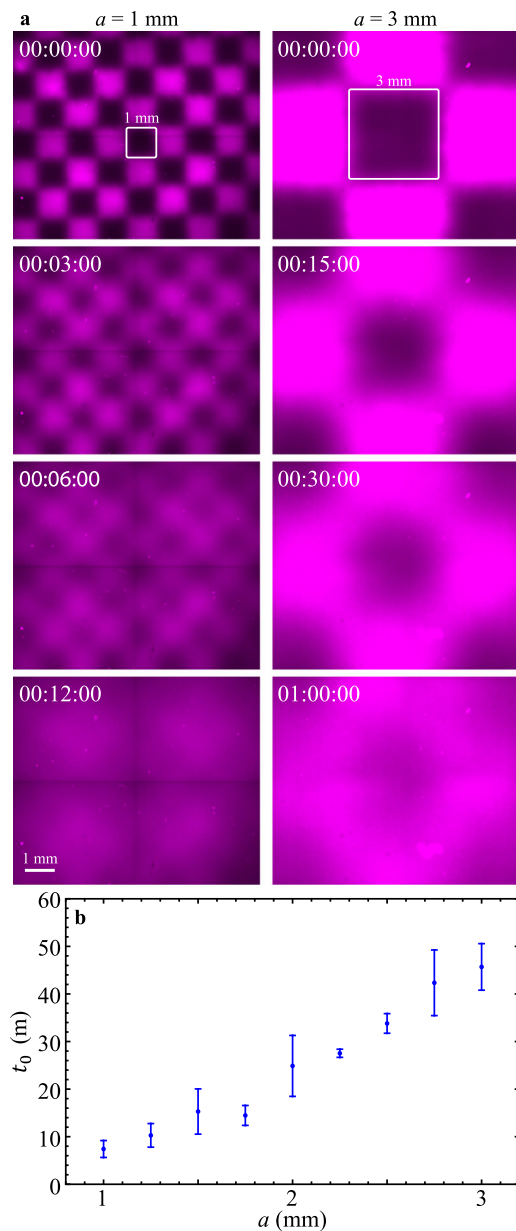
Fig. 7 | (Experimental results) Fluid activated in a checkerboard pattern mixes faster when the checkerboard grid is smaller. a Checkerboard-patterned UV lights are used to activate active fluid and caged fluorescent dyes. (Supplementary Movie 5). **b** The mixing time of the checkerboard-activated fluid increases with grid size, which demonstrates that the mixing efficacy of active fluid depends on distribution of activity: more nonuniform active fluid mixes the system more slowly. Each error bar in t_0 represents the standard deviation of two trials.

(Fig. 5c). Our simulation also shows that as ATP diffuses sufficiently fast ($D^* \gtrsim 32$; olive and red curves), the mixing time is nearly independent of activity level. Overall, increasing both the molecular diffusion coefficient and the activity level decreases mixing time. Thus, our simulation shows that both molecular diffusion (represented as D^*) and active fluid-induced convection (related to α_0^*) play important roles to disperse and homogenize the suspended components; which mechanism dominates the dispersion depends upon the competition between these two mechanisms.

To demonstrate how the competition of these two mechanisms affects the progression of active-inactive interfaces, we analyze the interface progression exponent γ as a function of α_0^* for various diffusion coefficients D^* (Fig. 6c inset) and find that when the diffusion

mechanism is relatively weak ($D^* = 2$; dark blue curve), the convection mechanism dominates the interface progression, leading it to progress in a superdiffusion-like, or more precisely, ballistic-like manner ($\gamma \approx 2$). Contrarily, as the diffusion mechanism becomes relatively strong ($D^* = 8$; light green curve), diffusion mechanisms dominate the interface progression, leading it to progress in a diffusion-like manner ($\gamma \approx 1$). Interestingly, we find that in an intermediate strength of diffusion mechanism ($D^* = 4$; dark green curve), increasing activity level α_0^* transitions the interface progression from diffusion-like to superdiffusion-like, which is consistent with our experimental observation (Fig. 4). Overall, our active-fluid hydrodynamic model qualitatively captures the mixing dynamics of active and inactive fluid systems in terms of active-inactive interface progression and dispersion of suspended components.

Checkered distribution of dyes and activity

Up until this point we have only explored one configuration of nonuniform active fluid systems: an activated bulk on one side of a channel adjacent to an inactive bulk on the other side. To explore how other spatial configurations of activity affect mixing, we use a checkerboard pattern of UV light to split the activated region into cells. As in previous experiments, 50% of the total fluid is activated. Fluid activated in a checkerboard pattern evolves to a homogeneous state more quickly than fluid that is activated on one side only (1 hour vs. 10 hours; Fig. 7a). UV-activated fluorescent dyes show that the mixing time decreases as the grid size decreases from 3 mm to 1 mm (Fig. 7b).

To elucidate how checkerboard mixing driven by active fluid differs from that driven by molecular diffusion alone, we apply our established active-fluid hydrodynamic model for both active ($\alpha^* = 25$) and inactive ($\alpha^* = 0$) fluid systems (Fig. 8a; Supplementary Movie 6). As expected, we find that the mixing time increases monotonically with grid size for both active and inactive fluid systems (Fig. 8b), with the active fluid system (red curve) having a shorter mixing time than the inactive fluid system (black curve). Interestingly, we find that when the grid size is sufficiently small ($a \lesssim 5$), the active and inactive fluids have the same simulated mixing time. We also find that as the grid size increases from 5 to 22, the mixing time of the inactive fluid increases more than the mixing time of the active fluid (40× vs. 3×).

Discussion

The self-mixing process of microtubule-kinesin active fluid with nonuniform activity is driven by active transport at the active-inactive interface. We estimate the contributions of diffusive and convective transport using the Péclet number, Pe. We find that when the active transport is dominated by the diffusion mechanism (Pe $\lesssim 3$), the active-inactive interface progresses in a diffusion-like manner ($\gamma \approx 1$; Fig. 2). These dynamics are quantitatively captured by a Fick's law-based model that quasi-statically related local activity to the local concentration of ATP by using a previously measured ATP-velocity relation (Fig. 3)[48].

As we raise the Péclet number (Pe $\gtrsim 3$) by increasing both the local fluid velocity and mixing length scale, we find that the active-inactive interface concomitantly progresses in a more superdiffusion-like manner ($\gamma > 1$; Fig. 4). We observe experimentally that increasing the Péclet number decreases the mixing time of suspended fluorescent dyes (Fig. 5c), which demonstrates that more convective flow mixes the suspended components faster. These results, along with the progression of the active-inactive interfaces, are qualitatively captured by an active-fluid hydrodynamic model (Fig. 6c) that couples active stress-induced fluid flow and transport of ATP molecules (Eqs. (6–9)).

Interestingly, while our hydrodynamic model predicts interface progression exponent $\gamma = 2$ for high activity levels (Fig. 6c inset), in our experiments γ appears to plateau at $\gamma \approx 1.7$ (Fig. 4b). Our model may have overestimated γ because the microtubule network in the inactive portion of the sample is crosslinked by immobile kinesin motor dimers
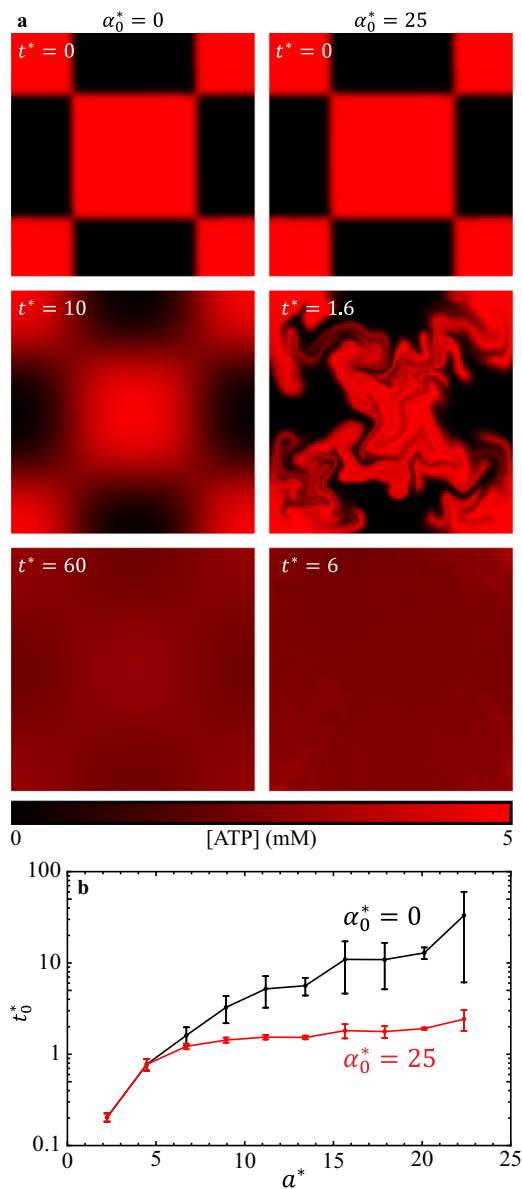
Fig. 8 | (Modeling results) Simulations with ATP initially distributed in a checkerboard pattern in a 45 × 45 simulation box. a Distributions of ATP (red) disperse from the checkerboard pattern (Eq. 11 with $a^* = 22$) to a homogeneous state by molecular diffusion only (left; $D^* = 1$, $\alpha_0^* = 0$) and by the combination of molecular diffusion and active fluid-induced convection (right; $D^* = 1$, $\alpha_0^* = 25$). **b** The dimensionless mixing time of ATP increases monotonically with the dimensionless checkerboard grid size a^* in both active (red) and inactive (black) fluid systems. Error bars represent the standard deviation of two trials performed with different types of checkerboard pattern (Eq. (11) and (12)).

that cause it to behave like an elastic gel. When the ATP molecules arrive at the active-inactive interface, they fuel the motor dimers, which fluidizes the network. Crucially, this fluidizing/melting process takes time to develop[47,50]. Thus, for the interface to progress, not only does ATP need to be transported to the inactive fluid region, but the ATP-fueled motors also need time to melt the gel-like microtubule network into a fluid. Such melting dynamics can delay the progression of the active-inactive interface and lower γ. In the simulation, the melting dynamics are absent; the network melts almost instantly as soon as ATP arrives at the inactive fluid, and γ only depends on active transport of ATP. Our additional studies (Supplementary Note 6) support the idea of a network melting mechanism by showing that the progression of the active-inactive interface falls behind the

progression of ATP molecules (Supplementary Fig. 7e), whereas in the simulation the fronts of both coincide (Supplementary Fig. 8c). Future research to elucidate the network melting dynamics can involve monitoring dyes, tracers, and microtubules simultaneously to reveal the correlations among ATP dispersion, active fluid flows, and microtubule network structure (melting). The process can be modeled with the active-fluid hydrodynamic model used herein, modified to include ATP-dependent rheological constants and additional relevant dynamic processes to represent the melting process of the gel-like network at the interface.

We also find that the distribution of activity has a significant effect on mixing time. Systems consisting of more, smaller active areas (checkerboard pattern; high uniformity (Fig. 7) evolve to a homogeneous state faster than systems with the same total active area distributed as one piece (one side active; low uniformity (Fig. 1c). This is likely because the smaller grid size increases the active-inactive interface area, which allows the active fluid to interact with inactive fluid more efficiently. Interestingly, our active-fluid hydrodynamic model shows that when the grid size is sufficiently small, the mixing times of active and inactive fluids are indistinguishable (Fig. 8b). This may be because the active fluid needs time to warm up from an initial quiescent state before reaching its steady activity state[47]. In experiments, the system has a warm-up time that may have been caused by network melting (Supplementary Note 6). Although a network melting mechanism is not included in the model, the simulated active fluid flow takes dimensionless time to rise because the onset of the flows is triggered by the initial activity-driven instability in extensile **Q** field, which takes finite dimensionless time to develop (~1 dimensionless time in this case; Supplementary Movie 6)[25,47]. Thus, in cases where the grid size is sufficiently small, the model shows molecular diffusion completing the mixing before emergence of active fluid flows. We also find that mixing time in an active fluid system is less sensitive to initial distribution of activity than that in an inactive system (Fig. 8b), which suggests that introducing active fluid to a microfluidic system can drastically reduce the impact of the initial condition on mixing efficacy.

This study has limitations. Observations on the mixing of active microtubule-kinesin fluid and inactive microtubule-kinesin fluid may not be generalizable to cases in which active fluid mixes with other types of fluid. Also, we do not characterize the degree of chaos in the system, such as by measuring Lyapunov exponents and topological entropies[24]. Future research can track tracers in 3D and measure how these quantities change in the 3D isotropic active microtubule network at different strengths of active transport (i.e., Lyapunov exponent vs. Péclet number and topological entropy vs. Péclet number).

Another limitation of this study is that our results for interface progression transitioning from diffusion-like to superdiffusion-like (Fig. 4) are based on large length-scale data that we analyze considering the interface as one piece with a specific position coordinate (Fig. 2a). However, the interface is the region where ATP concentration decays from saturation (>K; see Eq. (4)) to 0, and according to previous studies[14,35] tracer motion in this region should transition from superdiffusion-like to diffusion-like behaviors. Directly measuring the mean squared displacement of tracers across the active-inactive interface can elucidate the transition of the interface progression behaviors on the microscopic scale. Such measurements are not practical in our system because the active-inactive interface changes position and width with time (Fig. 1e); tracers initially in the diffusive zone can later be in the superdiffusive zone as the interface passes by, and it will be difficult to distinguish between the diffusive and superdiffusive data. Future research to elucidate tracer behaviors at active-inactive interfaces can utilize fluid that is only active when it is exposed to light[31,32] to provide a stable activity gradient and thus obtain a reliable mean squared displacement of tracers at different parts of the interface.

Overall, this work demonstrates that mixing in nonuniform active fluid systems is fundamentally different from mixing in uniform active fluids. Mixing in nonuniform active fluid systems involves complex interplays among spatial distribution of ATP, active transport of ATP (which can be either diffusion-like or convection-like, depending on Péclet number), and a fluid-gel transition of the microtubule network at the interface[47]. This work paves the path to the design of microfluidic devices that use active fluid to promote or optimize the micromixing process[8] to enhance production efficiency in chemical and biological engineering and pharmaceutical development[1]. The results may also provide insight into intracellular mixing processes, because the cytoplasmic streaming that supports organelles within cells is powered by cytoskeletal filaments and motor proteins that function similarly to microtubule-kinesin active fluid[61].

Methods

Polymerize microtubules

Microtubules constitute the underlying network of microtubule-kinesin active fluid. Microtubules are polymerized from bovine brain α- and β-tubulin dimers purified by three cycles of polymerization and depolymerization[62,63]. The microtubules (8 mg/mL) are then stabilized with 600 μM guanosine-5'[(α,β)-methyleno]triphosphate (GMPCPP, Jena Biosciences, NU-4056) and 1 mM dithiothreitol (DTT, Fisher Scientific, AC165680050) in microtubule buffer (80 mM PIPES, 2 mM MgCl₂, 1 mM ethylene glycol-bis(β-aminoethyl ether)-N,N,N',N'-tetraacetic acid, pH 6.8) and polymerized by a 30-minute incubation at 37 °C and a subsequent 6-hour annealing at room temperature before being snap frozen with liquid nitrogen and stored at −80 °C. The microtubules are then labeled with Alexa Fluor 647 (excitation: 650 nm; emission: 671 nm; Invitrogen, A-20006) and mixed with unlabeled microtubules at 3% labeling fraction during polymerization to image microtubules for non-fluorescein experiments (Figs. 1, 2, and 4). For fluorescein experiments, the microtubules are unlabeled (Figs. 5 and 7).

Dimerize kinesin motor proteins

Kinesin motor proteins power the extensile motion of sliding microtubule bundle pairs in active fluid by forming a dimer and walking on adjacent antiparallel microtubules to force them in opposite directions (Fig. 1a)[14,64]. We express kinesin in the *Escherichia coli* derivative Rosetta 2 (DE3) pLysS cells (Novagen, 71403), which we transform with DNA plasmids from *Drosophila melanogaster* kinesin (DMK) genes[65]. For most experiments in this paper, we use processive motors that include DMK's first 401 N-terminal DNA codons (K401)[66]. To explore the effect of low mean speed of active fluid bulk on the interface progression exponent γ, we mix in fractions of nonprocessive motors whose plasmid includes DMK's first 365 codons (K365, Fig. 4 inset left)[36,48,67]. The kinesin motors are tagged with 6 histidines enabling purification via immobilized metal ion affinity chromatography with gravity nickel columns (GE Healthcare, 11003399). To slide adjacent microtubule bundle pairs, kinesin motors need to be dimerized, so the kinesin motors are tagged with a biotin carboxyl carrier protein at their N terminals, which allow the kinesins to be bound with biotin molecules (Alfa Aesar, A14207)[14,62]. To dimerize the kinesin, we mix either 1.5 μM K401 processive motors or 5.4 μM K365 nonprocessive motors with 1.8 μM streptavidin (Invitrogen, S-888) and 120 μM DTT in microtubule buffer, incubate them for 30 minutes at 4 °C, and then snap freeze them with liquid nitrogen and store them at −80 °C.

Prepare microtubule-kinesin active fluid

To prepare the active fluid, we mix 1.3 mg/mL microtubules with 120 nM kinesin motor dimers and 0.8% polyethylene glycol (Sigma 81300), which acts as a depleting agent to bundle microtubules (Fig. 1a)[14]. Kinesin steps from the minus to the plus end of microtubules by hydrolyzing ATP and producing adenosine diphosphate[59]. To control the initial spatial distribution of ATP and thus the activity distribution of active fluid, we use 0.5 to 8 mM caged ATP (adenosine 5′-triphosphate, P3-(1-(4,5-dimethoxy-2-nitrophenyl)ethyl) ester, disodium salt and DMNPE-caged ATP, Fisher Scientific, A1049), which is ATP whose terminal phosphate is esterified with a blocking group rendering it nonhydrolyzable by kinesin motors unless exposed to 360-nm UV light. Exposure to UV light removes the blocking group (Fig. 1b) and allows the kinesin motors to hydrolyze the ATP into ADP and activate the active fluid[45,46]. The ATP hydrolyzation decreases ATP concentrations, which slow down the kinesin stepping rate and thus decrease active fluid flow speed[14,35,48,58,59]. To maintain ATP concentrations so as to stabilize the activity level of the active fluid bulk over the course of our experiments, we include 2.8% v/v pyruvate kinase/lactate dehydrogenase (Sigma, P-0294), which converts ADP back to ATP[14,68]. To feed the pyruvate kinase enzyme, we add 26 mM phosphenol pyruvate (BeanTown Chemical, 129745). We image the active fluid samples with fluorescent microscopy for 1 to 16 hours, which can bleach the fluorescent dyes and thus decrease the image quality over the course of experiments. To reduce the photobleaching effect, we include 2 mM trolox (Sigma, 238813) and oxygen-scavenging enzymes consisting of 0.038 mg/mL catalase (Sigma, C40) and 0.22 mg/mL glucose oxidase (Sigma, G2133) and feed the enzymes with 3.3 mg/mL glucose (Sigma, G7528)[14]. To stabilize proteins in our active fluid system, we add 5.5 mM DTT. To track the fluid flows, we dope the active fluid with 0.0016% v/v fluorescent tracer particles (Alexa 488-labeled [excitation: 499 nm; emission: 520 nm] 3-μm polystyrene microspheres, Polyscience, 18861). To test how active fluid can mix suspended components, we introduce 0.5 to 6 μM caged, UV-activated fluorescent dyes (fluorescein bis-(5-carboxymethoxy-2-nitrobenzyl) ether, dipotassium salt; CMNB-caged fluorescein, ThermoFisher Scientific, F7103), which are colorless and nonfluorescent until exposed to 360-nm UV light[45]. The dye concentration is chosen to maintain a sufficient signal-to-noise ratio while avoiding brightness saturation in micrographs. Upon UV exposure, the fluorescein is uncaged and thus becomes fluorescent and can be observed with fluorescent microscopy. Because the fluorescent spectrum of the fluorescein overlaps with our Alexa 488 tracers, for our experiments with caged fluorescein (Fig. 5) we replace the tracers with Flash Red-labeled 2-μm polystyrene microspheres (Bangs Laboratories, FSFR005) and use unlabeled microtubules (0% labeling fraction) to prevent fluorescent interference from microtubules while imaging tracers.

Prepare active-inactive fluid systems

To prepare the active-inactive fluid system, we load the inactive microtubule-kinesin fluid with caged ATP to a polyacrylamide-coated glass flow cell (20 × 4 × 0.1 mm³) with Parafilm (Cole-Parmer, EW-06720-40) as a spacer sandwiched between a cover slip (VWR, 48366-227) and slide (VWR, 75799-268)[36] and seal the channel with epoxy (Bob Smith Industries, BSI-201). Then we mask one side of the sample with a removable mask of opaque black tape (McMaster-Carr, 76455A21) attach to a transparent plastic sheet (Supplementary Fig. 9a) and shine UV light on the sample for 5 minutes before removing the mask (Supplementary Fig. 10). In the unmasked region, the UV light releases the ATP from the blocking group and activates the fluid by allowing the ATP to fuel the local kinesin motors; in the masked region, the fluid remains quiescent (Fig. 1c; Supplementary Movie 1)[45]. To explore how the progression exponent changes with active fluid bulk mean speed, we accelerate fluid flows by making the flow cell taller by stacking layers of Parafilm to decrease hydrodynamic resistance (Fig. 4a inset right)[48,52]. To explore how the spatial nonuniformity of activity influences the mixing efficacy of the active-inactive fluid system, we mask the sample with checkerboard-patterned masks (FineLine Imaging, Fig. 7a).

Image samples with dual fluorescent channels

We image the active fluids with epifluorescent microscopy (Ti2-E Inverted Microscope, Nikon, MEA54000) with the commercial image acquisition software Nikon NIS Elements version 5.11.03. To capture a wide area of the sample (20×4 mm^2), we use a $4\times$ objective lens (CFI Plan Apo Lambda $4\times$ Obj, Nikon, MRD00045, NA 0.2) to image 3 to 4 adjacent frames rapidly ($\lesssim 3$ s) and stitch the micrographs into one large image for flow and dye dispersion analyses (Figs. 1, 2, 4, 5, and 7; Supplementary Fig. 9b).

Performing these analyses requires monitoring at least two components in two fluorescent channels in each sample; for example, the dye dispersion experiments (Fig. 5) requires analyzing fluorescent dyes (excitation: 490 nm; emission: 525 nm) and Flash Red-labeled tracers (excitation: 660 nm; emission: 690 nm) simultaneously. This could have been accomplished by programming a microscope to rapidly switch back and forth between filter cubes, but this would have quickly worn down the turret motor and the time required to switch filter cubes (≥ 4 s) and move the stage to capture adjacent images and stitch them (~3 s) would have made the minimum time interval between frames ≥ 10 s, which would have prevented us from tracking high-density tracers (1000 mm^{-3} with a mean separation of 5 μm in a 0.1-mm-thick sample) whose speeds are 1 to 10 μm/s, even with a predictive Lagrangian tracking algorithm[69]. To overcome this technical challenge in imaging our samples, we establish a dual-channel imaging system that consisted of a multiband pass filter cube (Multi LED set, Chroma, 89402–ET) and voltage trigger (Nikon) placed between the light source (pE-300$^{\text{ultra}}$, CoolLED, BU0080) and camera (Andor Zyla, Nikon, ZYLA5.5-USB3). Instead of changing filter cubes, the multiband pass filter cube allows us to switch between multiple emission and excitation bands by switching between channels with the same filter cube. We alternatively activate the blue (401–500 nm) and red (500–700 nm) LEDs to excite and observe the fluorescent dyes and tracers almost simultaneously. The LED light source communicates directly with the camera via voltage triggering to coordinate LED activation time and bypass computer control to further boost the light switching rate. This technique shortens our channel switching time to 3 to 5 μs; thus the time interval between image acquisitions of different fluorescent channels is only limited by the exposure times of each channel. This setup allows us to image two fluorescent channels almost simultaneously (within milliseconds) and thus enables us to monitor two fluorescent components side-by-side, such as microtubules and tracers (Fig. 1c; Supplementary Movie 1), caged fluorescent dyes and tracers (Fig. 5c), and caged fluorescent dyes and microtubules (Supplementary Movie 5).

Analyze positions of active-inactive fluid interfaces

We characterize the mixing kinematics of active and inactive fluids by analyzing the interface progression exponents γ and coefficients P_{I} (Figs. 2–4). These analyses require identification of the interface positions. We determine the interface positions by first tracking tracers in sequential images with the Lagrangian tracking algorithm[69], which reveals the tracers' trajectories $r_i(t)$ and corresponding instantaneous velocities $v_i \equiv dr_i/dt$. Then we analyze the speed profile of tracers by binning the tracer speed $|v_i|$ across the width of the channel $S(x_j) \equiv \langle |v_i| \rangle_{i \in \text{bin } j}$ where x_j is the horizontal x coordinate of the jth bin and the $\langle |v_i| \rangle_{i \in \text{bin } j}$ represents the average speed of tracers in the jth bin. Then we normalize the speed profile by rescaling the speed profile to be 1 in the active zone and 0 in the inactive zone: $S^*(x) \equiv [S(x) - s_{\text{in}}] / [s_{\text{a}} - s_{\text{in}}]$, where s_{a} is the average of speed profiles in the active zone and s_{in} is the average of speed profiles in the inactive zone (Fig. 1e). Then we define the width of the active-inactive fluid interface as where the normalized speed profile is between 0.2 and 0.8 (dashed lines in Fig. 1e inset) and the position of the interface x_{I} as where the normalized speed profile is 0.5 (solid line). The interface position is then analyzed for each frame, which allows us to determine

the interface displacement $\Delta x \equiv x_{\text{I}}(\Delta t) - x_{\text{I}}(0)$ vs. time t (Fig. 2a inset) and the squared interface displacement Δx^2 vs. time t (Fig. 2a). To determine the interface progression exponent, γ, we fit $\log(\Delta x^2)$ vs. $\log(t)$ data to $\log(\Delta x^2) = \log(2P_{\text{I}}) + \gamma \log(t)$, with P_{I} and γ as fitting parameters (Figs. 2b and 4). To determine the interface progression coefficient, P_{I}, we assume $\gamma = 1$ and fit Δx^2 vs. t data to $\Delta x^2 = 2P_{\text{I}}t$ with P_{I} as the fitting parameter (Figs. 2c, 3c, d).

Generate flow speed map of active-inactive fluid system

To visualize the activity distribution in our active-inactive fluid system, we analyze the distribution of flow speed to generate flow speed maps (Fig. 1d). To complete this analysis, we analyze the flow velocities of fluids by analyzing the tracer motions in sequential images with a particle image velocimetry algorithm[70], which reveals the flow velocity field $\mathbf{V}(\mathbf{r},t)$ and associated distribution of flow speed $|\mathbf{V}(\mathbf{r},t)|$ in each frame. A heat color bar (Fig. 1d) is used to plot the speed distributions into color maps to reveal the evolution of speed distribution from the pre-activated state (black) to the homogeneously activated state (red/yellow).

Numerically solve the Fick's law equations

We model diffusion-dominated active-inactive fluid mixing with the Fick's law equation, which requires us to solve for the concentration of ATP (Eq. (1)). To simplify the modeling, we consider a one-dimensional active fluid system confined in a segment $x = 0-L$ where $L = 20$ mm, the length of our experimental sample. Given that ATP is confined in the segment, we apply no-flux boundary conditions to the ATP concentrations (Eq. (2)). In the experiment, we expose the left side of the sample to UV light to release ATP, so in our model the ATP concentration has a step function as its initial condition (Eq. (3)). With the initial condition and boundary conditions, we solve the Fick's law equation to determine the spatial and temporal distribution of ATP. We used Mathematica 13.0 to numerically solve this differential equation with the NDSolveValue function by feeding Eqs. (1–3) into the function followed by specifying the spatial and temporal domains, which outputs the numerical solution of ATP concentration $C(x,t)$ and allows us to determine the evolution of ATP distribution (Fig. 3a). Then we convert the ATP distribution to mean speed distribution of active fluid by the Michaelis-Menten kinetics (Eq. (4); Fig. 3b inset), which shows a uniform mean speed in the left side of the sample followed by gradual activation of the right side of the system until a uniform state is reached (Fig. 3b). Then we define the position of the active-inactive fluid interface Δx as where the mean speed decays to a half (Fig. 3c inset), which allows us to plot the squared interface displacement as a function of time (Fig. 3c). The plot in log-log axes exhibits a line with a unit slope, which suggests that the squared interface displacement is linearly proportional to time. By assuming this linear relation, we determine the interface progression coefficient P_{I} by fitting $\Delta x^2 = 2P_{\text{I}}t$ with P_{I} as the fitting parameter. Finally, we repeat the calculation with different initial ATP concentrations in the left side of the system, C_0, and plot the interface progression coefficient, P_{I}, as a function of C_0. This plot allows us to compare the simulation results with the experimental measurements to examine the validity of our Fick's law-based model (Fig. 3d).

Numerically solve the active nematohydrodynamic equations

To model the mixing of active and inactive fluids, we adopt Varghese et al.'s active fluid model to include the dynamics of the ATP concentration field[22]. Our model has four main components: (1) the kinetic equation describing the kinematics of self-elongating rods that flow and orient with the solvent as well as diffuse translationally and rotationally (Eqs. 6), (2) the Stokes equation describing how the solvent is driven by the active stress exerted by the self-elongating rods (Eqs. 7), (3) the relation between α and ATP that describes how the active stress depends on the nonuniform ATP distribution (Eqs. (8)), and (4) the

continuity equation of ATP transport that describes how ATP diffuses as well as flows with the solvent (Eq. (9)). We numerically solve these coupled equations with appropriate boundary and initial conditions using the finite element method by first converting them to their weak forms and then implementing them symbolically in COMSOL Multiphysics™ [60]. We show below the weak form of the convection-diffusion equation governing the evolution of ATP concentration field:

$$\int_\Gamma dx^* dy^* \tilde{T} \frac{\partial C}{\partial t^*} = -\int_\Gamma dx^* dy^* D^* \left(\frac{\partial \tilde{T}}{\partial x^*} \frac{\partial C}{\partial x^*} + \frac{\partial \tilde{T}}{\partial y^*} \frac{\partial C}{\partial y^*} \right) \\ - \int_\Gamma dx^* dy^* \tilde{T} \left(u_x^* \frac{\partial C}{\partial x^*} + u_y^* \frac{\partial C}{\partial y^*} \right),$$

(10)

where $\tilde{T}(x^*, y^*)$ is the test function and Γ represents the system spatial domain. After solving these equations, we determine the spatial and temporal distributions of ATP concentrations and active fluid flow speeds (Fig. 6a and Supplementary Movie 4), which allows us to explore how the activity level of active fluid and molecular diffusion of ATP influences the mixing process of ATP in nonuniform active fluid systems (Fig. 6b, c).

Simulate dispersion of checkerboard-patterned ATP

We apply our established hydrodynamic model to simulate how the initially checkerboard-patterned ATP disperses in active fluid and inactive fluid (Fig. 8). In this exploration, we use the same equations for **Q**, **u** and C (Eqs. (6–9)), along with their initial and boundary conditions, except that C is initialized in a checkerboard pattern in a 45×45 simulation box. We use two different checkerboard patterns for different trials. One has the xy-axis origin in the center of a grid square:

$$C(x,y,t=0) = C_0 \bmod \left\{ \bmod \left[\text{ceil}\left(\frac{x^*}{a^*} - 0.5 \right), 2 \right] + \bmod \left[\text{ceil}\left(\frac{y^*}{a^*} - 0.5 \right), 2 \right] + 1, 2 \right\},$$

(11)

where $C_0 = 5$ mM is the initial ATP concentration, a^* represents the dimensionless grid size of the checkerboard pattern, $\bmod(i,j)$ represents the remainder of i divided by j, and $\text{ceil}(x)$ represents the rounding of x toward positive infinity (e.g., Fig. 8a with $a^* = 22$). The other checkerboard pattern has the xy-axis origin at a vertex of the grid:

$$C(x,y,t=0) = C_0 \bmod \left\{ \bmod \left[\text{ceil}\left(\frac{x^*}{a^*} \right), 2 \right] + \bmod \left[\text{ceil}\left(\frac{y^*}{a^*} \right), 2 \right] + 1, 2 \right\}.$$

(12)

The simulation is performed for the dimensionless grid size a^* ranging from 2 to 22 for both active ($\alpha^* = 25$) and inactive ($\alpha^* = 0$) systems (Fig. 8a). We analyze the corresponding mixing time (averaged over 2 trials) as a function of a^* (Fig. 8b) to reveal how the a^*-dependence of mixing times differs in active and inactive fluid systems.

Data availability

The datasets generated and analyzed during the current study are available in the figshare repository, https://doi.org/10.6084/m9.figshare.21358017, or available from the corresponding author on request.

Code availability

The Mathematica script used to solve the Fick's law-based model (Eqs. (1–4)) and the COMSOL file used to solve the active nemathydrodynamic equations coupled with active transport of ATP (Eqs. (6–9)) has been deposited on figshare (https://doi.org/10.6084/m9.figshare.20332806).

References

1. Jeong, G. S., Chung, S., Kim, C.-B. & Lee, S.-H. Applications of micromixing technology. *Analyst* **135**, 460–473 (2010).
2. Haswell, S. J. et al. The application of micro reactors to synthetic chemistry. *Chem. Commun.* **2001**, 391–398 (2001).
3. Hadd, A. G., Raymond, D. E., Halliwell, J. W., Jacobson, S. C. & Ramsey, J. M. Microchip device for performing enzyme assays. *Anal. Chem.* **69**, 3407–3412 (1997).
4. Kakuta, M., Jayawickrama, D. A., Wolters, A. M., Manz, A. & Sweedler, J. V. Micromixer-based time-resolved NMR: Applications to ubiquitin protein conformation. *Anal. Chem.* **75**, 956–960 (2003).
5. Ottino, J. M. Mixing, chaotic advection, and turbulence. *Annu Rev. Fluid Mech.* **22**, 207–254 (1990).
6. Suzuki, H., Chih-Ming, H. & Kasagi, N. A chaotic mixer for magnetic bead-based micro cell sorter. *J. Microelectromech Syst.* **13**, 779–790 (2004).
7. Liu, R. H., Yang, J., Pindera, M. Z., Athavale, M. & Grodzinski, P. Bubble-induced acoustic micromixing. *Lab Chip* **2**, 151–157 (2002).
8. Ober, T. J., Foresti, D. & Lewis, J. A. Active mixing of complex fluids at the microscale. *Proc. Natl Acad. Sci. USA* **112**, 12293–12298 (2015).
9. Ramaswamy, S. Active fluids. *Nat. Rev. Phys.* **1**, 640–642 (2019).
10. Marchetti, M. C. et al. Hydrodynamics of soft active matter. *Rev. Mod. Phys.* **85**, 1143–1189 (2013).
11. Needleman, D. & Dogic, Z. Active matter at the interface between materials science and cell biology. *Nat. Rev. Mater.* **2**, 17048 (2017).
12. Sokolov, A., Apodaca, M. M., Grzybowski, B. A. & Aranson, I. S. Swimming bacteria power microscopic gears. *Proc. Natl Acad. Sci. USA* **107**, 969–974 (2010).
13. Lushi, E., Wioland, H. & Goldstein, R. E. Fluid flows created by swimming bacteria drive self-organization in confined suspensions. *Proc. Natl Acad. Sci. USA* **111**, 9733–9738 (2014).
14. Sanchez, T., Chen, D. T. N., DeCamp, S. J., Heymann, M. & Dogic, Z. Spontaneous motion in hierarchically assembled active matter. *Nature* **491**, 431–434 (2012).
15. Palacci, J., Sacanna, S., Steinberg, A. P., Pine, D. J. & Chaikin, P. M. Living crystals of light-activated colloidal surfers. *Science* **339**, 936–940 (2013).
16. Gompper, G. et al. The 2020 motile active matter roadmap. *J. Phys. Condens Matter* **32**, 193001 (2020).
17. Reinken, H. et al. Organizing bacterial vortex lattices by periodic obstacle arrays. *Commun. Phys.* **3**, 76 (2020).
18. Chen, Y.-C., Jolicoeur, B., Chueh, C.-C. & Wu, K.-T. Flow coupling between active and passive fluids across water–oil interfaces. *Sci. Rep.* **11**, 13965 (2021).
19. Thampi, S. P. & Yeomans, J. M. Active turbulence in active nematics. *Eur. Phys. J. Spec. Top.* **225**, 651–662 (2016).
20. Wensink, H. H. et al. Meso-scale turbulence in living fluids. *Proc. Natl Acad. Sci. USA* **109**, 14308–14313 (2012).
21. Doostmohammadi, A., Shendruk, T. N., Thijssen, K. & Yeomans, J. M. Onset of meso-scale turbulence in active nematics. *Nat. Commun.* **8**, 15326 (2017).
22. Alert, R., Joanny, J.-F. & Casademunt, J. Universal scaling of active nematic turbulence. *Nat. Phys.* **16**, 682–688 (2020).
23. Qi, K., Westphal, E., Gompper, G. & Winkler, R. G. Emergence of active turbulence in microswimmer suspensions due to active hydrodynamic stress and volume exclusion. *Commun. Phys.* **5**, 49 (2022).
24. Tan, A. J. et al. Topological chaos in active nematics. *Nat. Phys.* **15**, 1033–1039 (2019).
25. Saintillan, D. & Shelley, M. J. Instabilities, pattern formation, and mixing in active suspensions. *Phys. Fluids* **20**, 123304 (2008).

26. Kim, M. J. & Breuer, K. S. Enhanced diffusion due to motile bacteria. *Phys. Fluids* **16**, L78–L81 (2004).

27. del Junco, C., Estevez-Torres, A. & Maitra, A. Front speed and pattern selection of a propagating chemical front in an active fluid. *Phys. Rev. E* **105**, 014602 (2022).

28. Vyborna, Y., Galas, J.-C. & Estevez-Torres, A. DNA-controlled spatiotemporal patterning of a cytoskeletal active gel. *J. Am. Chem. Soc.* **143**, 20022–20026 (2021).

29. Wysocki, A., Winkler, R. G. & Gompper, G. Propagating interfaces in mixtures of active and passive Brownian particles. *N. J. Phys.* **18**, 123030 (2016).

30. Blow, M. L., Thampi, S. P. & Yeomans, J. M. Biphasic, lyotropic, active nematics. *Phys. Rev. Lett.* **113**, 248303 (2014).

31. Ross, T. D. et al. Controlling organization and forces in active matter through optically defined boundaries. *Nature* **572**, 224–229 (2019).

32. Zhang, R. et al. Spatiotemporal control of liquid crystal structure and dynamics through activity patterning. *Nat. Mater.* **20**, 875–882 (2021).

33. Shankar, S. & Marchetti, M. C. Hydrodynamics of active defects: From order to chaos to defect ordering. *Phys. Rev. X* **9**, 041047 (2019).

34. Norton, M. M., Grover, P., Hagan, M. F. & Fraden, S. Optimal control of active nematics. *Phys. Rev. Lett.* **125**, 178005 (2020).

35. Henkin, G., DeCamp, S. J., Chen, D. T. N., Sanchez, T. & Dogic, Z. Tunable dynamics of microtubule-based active isotropic gels. *Philos. Trans. A Math. Phys. Eng. Sci.* **372**, 20140142 (2014).

36. Chandrakar, P. et al. Engineering stability, longevity, and miscibility of microtubule-based active fluids. *Soft Matter* **18**, 1825–1835 (2022).

37. Tayar, A. M., Hagan, M. F. & Dogic, Z. Active liquid crystals powered by force-sensing DNA-motor clusters. *Proc. Natl Acad. Sci. USA* **118**, e2102873118 (2021).

38. Duclos, G. et al. Topological structure and dynamics of three-dimensional active nematics. *Science* **367**, 1120–1124 (2020).

39. Fan, Y., Wu, K.-T., Aghvami, S. A., Fraden, S. & Breuer, K. S. Effects of confinement on the dynamics and correlation scales in kinesin-microtubule active fluids. *Phys. Rev. E* **104**, 034601 (2021).

40. Lemma, L. M. et al. Multiscale microtubule dynamics in active nematics. *Phys. Rev. Lett.* **127**, 148001 (2021).

41. Gao, T., Blackwell, R., Glaser, M. A., Betterton, M. D. & Shelley, M. J. Multiscale polar theory of microtubule and motor-protein assemblies. *Phys. Rev. Lett.* **114**, 048101 (2015).

42. Thampi, S. P., Golestanian, R. & Yeomans, J. M. Vorticity, defects and correlations in active turbulence. *Philos. Trans. A Math. Phys. Eng. Sci.* **372**, 20130366 (2014).

43. Doostmohammadi, A., Ignés-Mullol, J., Yeomans, J. M. & Sagués, F. Active nematics. *Nat. Commun.* **9**, 3246 (2018).

44. Vliegenthart, G. A., Ravichandran, A., Ripoll, M., Auth, T. & Gompper, G. Filamentous active matter: Band formation, bending, buckling, and defects. *Sci. Adv.* **6**, eaaw9975 (2020).

45. Berezney, J., Goode, B. L., Fraden, S. & Dogic, Z. Extensile to contractile transition in active microtubule-actin composites generates layered asters with programmable lifetimes. *Proc. Natl Acad. Sci. USA* **119**, e2115895119 (2022).

46. McCray, J. A., Herbette, L., Kihara, T. & Trentham, D. R. A new approach to time-resolved studies of ATP-requiring biological systems; laser flash photolysis of caged ATP. *Proc. Natl Acad. Sci. USA* **77**, 7237–7241 (1980).

47. Najma, B. et al. Dual antagonistic role of motor proteins in fluidizing active networks. *arXiv:2112.11364 [cond-mat.soft]*. (2021).

48. Bate, T. E., Jarvis, E. J., Varney, M. E. & Wu, K.-T. Collective dynamics of microtubule-based 3D active fluids from single microtubules. *Soft Matter* **15**, 5006–5016 (2019).

49. Bowen, W. J. & Martin, H. L. The diffusion of adenosine triphosphate through aqueous solutions. *Arch. Biochem Biophys.* **107**, 30–36 (1964).

50. Gagnon, D. A. et al. Shear-induced gelation of self-yielding active networks. *Phys. Rev. Lett.* **125**, 178003 (2020).

51. Varghese, M., Baskaran, A., Hagan, M. F. & Baskaran, A. Confinement-induced self-pumping in 3D active fluids. *Phys. Rev. Lett.* **125**, 268003 (2020).

52. Wu, K.-T. et al. Transition from turbulent to coherent flows in confined three-dimensional active fluids. *Science* **355**, eaal1979 (2017).

53. Tuval, I. et al. Bacterial swimming and oxygen transport near contact lines. *Proc. Natl Acad. Sci. USA* **102**, 2277–2282 (2005).

54. Senoussi, A., Galas, J.-C. & Estevez-Torres, A. Programmed mechano-chemical coupling in reaction-diffusion active matter. *Sci. Adv.* **7**, eabi9865 (2021).

55. Aditi Simha, R. & Ramaswamy, S. Hydrodynamic fluctuations and instabilities in ordered suspensions of self-propelled particles. *Phys. Rev. Lett.* **89**, 058101 (2002).

56. Guillamat, P., Hardoüin, J., Prat, B. M., Ignés-Mullol, J. & Sagués, F. Control of active turbulence through addressable soft interfaces. *J. Phys. Condens Matter* **29**, 504003 (2017).

57. Lemma, L. M., Decamp, S. J., You, Z., Giomi, L. & Dogic, Z. Statistical properties of autonomous flows in 2D active nematics. *Soft Matter* **15**, 3264 (2019).

58. Coy, D. L., Wagenbach, M. & Howard, J. Kinesin takes one 8-nm step for each ATP that it hydrolyzes. *J. Biol. Chem.* **274**, 3667–3671 (1999).

59. Schnitzer, M. J. & Block, S. M. Kinesin hydrolyses one ATP per 8-nm step. *Nature* **388**, 386–390 (1997).

60. Bendaraa, A., Charafi, M. M. & Hasnaoui, A. Numerical study of natural convection in a differentially heated square cavity filled with nanofluid in the presence of fins attached to walls in different locations. *Phys. Fluids* **31**, 052003 (2019).

61. Woodhouse, F. G. & Goldstein, R. E. Cytoplasmic streaming in plant cells emerges naturally by microfilament self-organization. *Proc. Natl Acad. Sci. USA* **110**, 14132–14137 (2013).

62. Bate, T. E., Jarvis, E. J., Varney, M. E. & Wu, K.-T. Controlling flow speeds of microtubule-based 3D active fluids using temperature. *J. Vis. Exp.* **26**, e60484 (2019).

63. Castoldi, M. & Popov, A. V. Purification of brain tubulin through two cycles of polymerization–depolymerization in a high-molarity buffer. *Protein Expr. Purif.* **32**, 83–88 (2003).

64. Ndlec, F. J., Surrey, T., Maggs, A. C. & Leibler, S. Self-organization of microtubules and motors. *Nature* **389**, 305–308 (1997).

65. Baneyx, F. Recombinant protein expression in Escherichia coli. *Curr. Opin. Biotechnol.* **10**, 411–421 (1999).

66. Martin, D. S., Fathi, R., Mitchison, T. J. & Gelles, J. FRET measurements of kinesin neck orientation reveal a structural basis for processivity and asymmetry. *Proc. Natl Acad. Sci. USA* **107**, 5453–5458 (2010).

67. Young, E. C., Mahtani, H. K. & Gelles, J. One-headed kinesin derivatives move by a nonprocessive, low-duty ratio mechanism unlike that of two-headed kinesin. *Biochemistry* **37**, 3467–3479 (1998).

68. Chen, D. T. N., Heymann, M., Fraden, S., Nicastro, D. & Dogic, Z. ATP consumption of eukaryotic flagella measured at a single-cell level. *Biophys. J.* **109**, 2562–2573 (2015).

69. Ouellette, N. T., Xu, H. & Bodenschatz, E. A quantitative study of three-dimensional Lagrangian particle tracking algorithms. *Exp. Fluids* **40**, 301–313 (2005).

70. Thielicke, W. & Stamhuis, E. J. PIVlab–towards user-friendly, affordable and accurate digital particle image velocimetry in MATLAB. *J. Open Res Softw.* **2**, e30 (2014).

Author contributions

T.E.B., M.E.V., and K.-T.W. performed the research and designed the experiments; M.E.V. initiated the experiments; T.E.B., M.E.V., E.H.T. and J.H.D. collected experimental data; T.E.B., M.E.V., and K.-T.W. organized and analyzed the data; T.E.B., E.H.T., C.-C.C., M.M.N. and K.-T.W. established the continuum simulation platform on modeling nonuniform active fluid systems; T.E.B. and K.-T.W. wrote the manuscript; and K.-T.W. supervised the research. All authors reviewed the manuscript.

Competing interests

The authors declare no competing interests.

Additional information

Supplementary information The online version contains supplementary material available at https://doi.org/10.1038/s41467-022-34396-1.

Correspondence and requests for materials should be addressed to Kun-Ta Wu.

Peer review information *Nature Communications* thanks Linda Hirst and the other anonymous reviewer(s) for their contribution to the peer review of this work. Peer reviewer reports are available.

Reprints and permissions information is available at http://www.nature.com/reprints

Publisher's note Springer Nature remains neutral with regard to jurisdictional claims in published maps and institutional affiliations.

Supplementary Information:

Self-mixing in microtubule-kinesin active fluid from nonuniform to uniform distribution of activity

Teagan E Bate[1], Megan E Varney[2], Ezra H Taylor[1], Joshua H Dickie[1], Chih-Che Chueh[3], Michael M Norton[4], and Kun-Ta Wu[1,5,6,*]

[1] Department of Physics, Worcester Polytechnic Institute, Worcester, Massachusetts 01609, USA
[2] Department of Physics, New York University, New York, New York 10003, USA
[3] Department of Aeronautics and Astronautics, National Cheng Kung University, Tainan 701, Taiwan
[4] School of Physics and Astronomy, Rochester Institute of Technology, Rochester, New York 14623, USA
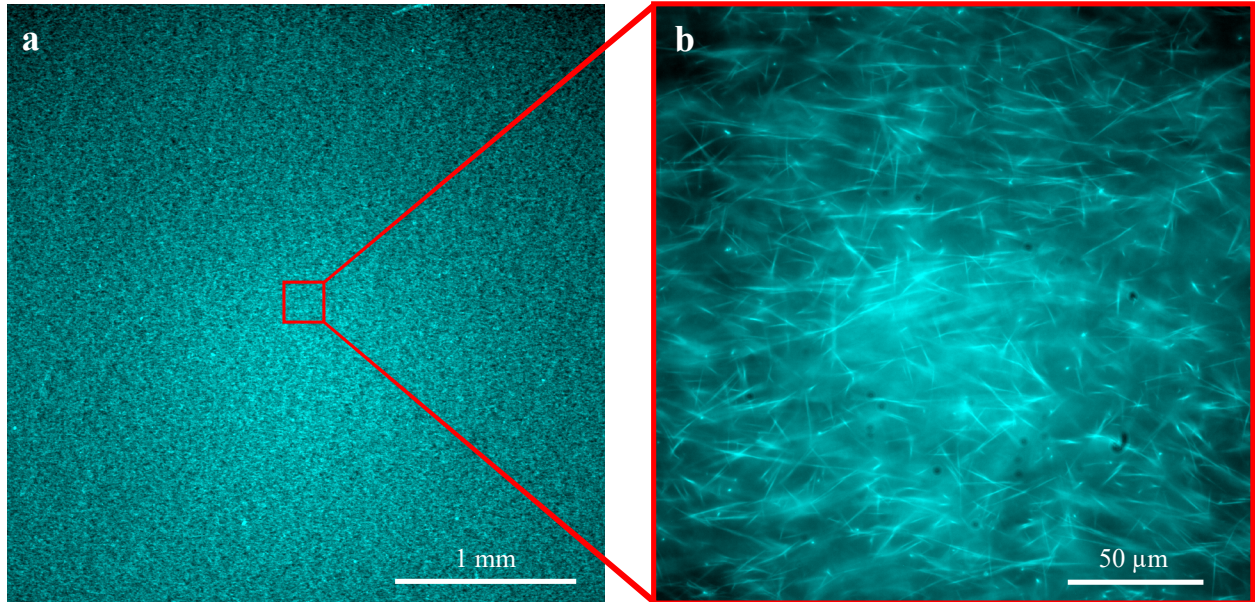[5] Department of Mechanical Engineering, Worcester Polytechnic Institute, Worcester, Massachusetts 01609, USA
[6] The Martin Fisher School of Physics, Brandeis University, Waltham, Massachusetts 02454, USA
*Corresponding: kwu@wpi.edu

Table of Contents

Supplementary Figure 1: (Experimental results) Microtubules in inactive fluid loaded into the flow cell before UV activation. (a) Micrograph of microtubules at millimeter scale. (b) Micrograph of microtubules at micrometer scale, showing an initial dominant alignment of microtubules parallel to the long edge of the flow cell (horizontal direction) caused by the shear flow induced by pipetting the sample into the cell.[1]

Supplementary Note 1: Estimation of ATP molecular diffusion coefficient in crosslinked microtubule networks

ATP molecular diffusion plays an important role in our characterization of active-inactive fluid mixing. For example, we characterize the dominant mechanism in active transport (i.e., diffusion or convection) by introducing the Péclet number, Pe (Figs. 4 & 5),[2,3] which depends on the molecular diffusion coefficient of ATP. We also adopt Fick's law (Eq. 1) to model the dispersion of ATP in low Pe regimes (Fig. 3), which also requires the ATP diffusion coefficient. As such, it is important to determine the molecular diffusion coefficient of ATP. It is challenging to directly observe the diffusion of ATP, but fluorescein can be directly visualized, and thus we analyze the molecular diffusion coefficient of fluorescein in the inactive microtubule network as the basis for estimating the molecular diffusion coefficient of ATP in our active fluid system.

We observe and characterize the dispersion of fluorescein near the interface of caged and UV-uncaged fluorescein suspended in inactive microtubule-kinesin fluid (Fig. 5a, Supplementary Figure 2a) and compare the observation with the solution of Fick's law (Eq. 1) to extract the corresponding molecular diffusion coefficient. For each micrograph, we average the gray values vertically to determine the gray value profile (Supplementary Figure 2b). We assume that the fluorescein concentration is proportional to the gray values, and thus the profiles of gray values should satisfy the Fick's law equation (Eq. 1), whose solution in a boundless 1D system takes the form of a complementary error function:

$$C(x,t) = \frac{C_0}{2}\,\text{erfc}\left(\frac{x - x_0}{2\sqrt{D(t - t_0)}}\right),$$

$$1$$

where C_0 is the initial concentration of the suspended molecules, erfc is the complementary error function, and D is the molecular diffusion coefficient of the suspended molecules. Thus, the profiles of gray values (G.V.) should take the form of

$$\text{G.V.}(x,t) = g_0\,\text{erfc}\left(\frac{x - x_0}{2\sqrt{\Gamma(t)}}\right) + g_0',$$

$$2$$

where g_0 is the prefactor and $\Gamma \equiv D(t - t_0)$. We add the constant g_0' to represent the gray value contributed from the background light in the microscope room. Then we fit this form to the profiles of gray values with g_0, g_0', x_0, and Γ as fitting parameters (Supplementary Figure 2b inset). The fit Γ is expected to be linear to time t, so we plot Γ as a function of time t and fit Γ vs. t to $\Gamma = D(t - t_0)$ with D and t_0 as fitting parameters (Supplementary Figure 2c), which reveals that the molecular diffusion coefficient of fluorescein in our inactive microtubule-kinesin system is $D = 97.4 \pm 0.2$ μm²/s. This analyzed diffusion coefficient is one-fifth the value reported in aqueous solution (400-600 μm²/s).[4-7] We attribute this discrepancy to the rheologically complex environment of the inactive fluid that results from crosslinked microtubules.[8] We assume that the molecular diffusion of ATP molecules is similarly diminished in our experiments. The reported diffusion coefficient of ATP in water is 710 μm²/s,[9] and we therefore estimate the diffusivity of ATP to be 140 μm²/s in our models and calculations (Figs. 3-5).
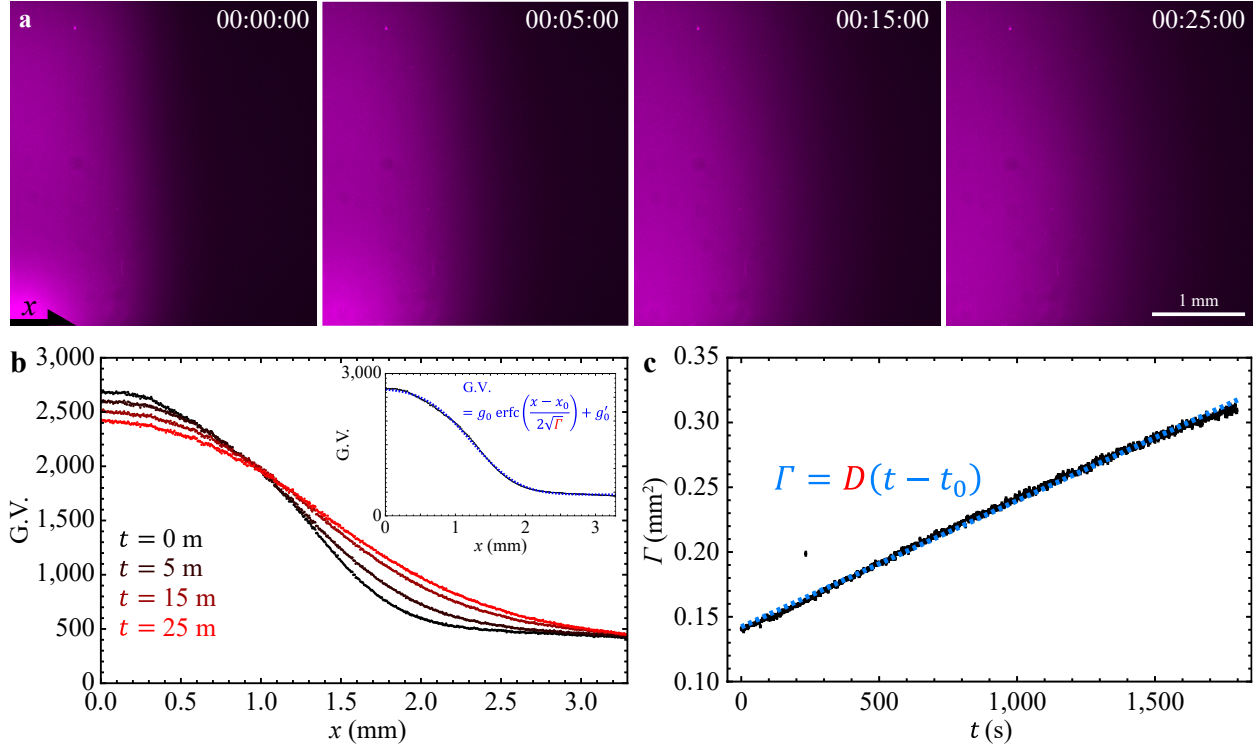
Supplementary Figure 2: (Experimental results) Analysis of molecular diffusion coefficient of fluorescein suspended in inactive microtubule-kinesin fluid. The fluorescein is caged such that it only fluoresces after exposure to ultraviolet light (Fig. 5a). (a) Micrographs of fluorescein near the edge of the ultraviolet light-exposed area. The time stamps indicate hour:minute:second. (b) Profiles of gray values in the micrographs shown in Panel a. Inset: The gray value profile of the micrograph at time 00:00:00 (black dots) is fit to a complementary error function (Supplementary Equation 2; blue dashed curve) to extract the parameter Γ which is expected to linearly increase with time t. (c) The fit parameter Γ as a function of time t (black dots) is fit to a line function (blue dashed line). The fit slope, $D = 97.4 \pm 0.2$ μm^2/s, represents the molecular diffusion coefficient of fluorescein suspended in crosslinked microtubule networks.

Supplementary Note 2: Effect of flow speed-ATP relation on active-inactive interface progression in the Fick's law-based model

We develop the Fick's law-based model (Fig. 3) to describe the experimentally observed mixing of active and inactive fluids (Fig. 2). Our model uses Michaelis-Menten kinetics to convert distribution of ATP to flow speed (Eq. 4) because flow speed is driven by microtubule motion, which in turn depends on the stepping rate of kinesin motors which follows Michaelis-Menten kinetics.[10-12] Our previous work shows that Michaelis-Menten kinetics reasonably connect flow speed of active fluid with ATP concentrations when the ATP concentration is above 100 μM.[13] Below this concentration, inactive kinesin motor dimers start to act as a crosslinkers in the microtubule network, causing the network to behave more like an elastic gel, and Michaelis-Menten kinetics fail to describe the flow speed because Michaelis-Menten kinetics is an enzyme-based model that does not consider network rheology.

As such, our adoption of Michaelis-Menten kinetics to convert ATP concentration to flow speed is an approximation for active fluid with high ATP concentrations ($\gtrsim$100 μM), and it is unclear how the results of our Fick's law-based model will change if we choose a different relation between ATP concentration and flow speed. Here we consider that the flow speed is connected to ATP concentration via a positive power-law exponent, $n > 0$, of the Michaelis-Menten relation:

$$\bar{v} = \bar{v}_{\mathrm{m}} \left(\frac{C}{C + K} \right)^n, \qquad\qquad 3$$

where $\bar{v}_{\mathrm{m}} = 6.2$ μm/s is the saturated mean speed of active fluid and $K = 270$ μM is the ATP concentration that leads to half of the saturated mean speed, $\bar{v}_{\mathrm{m}}/2$ (Supplementary Figure 3a).[13] Then we explore how n will affect the predicted active-inactive interface progression in terms of progression exponent γ and coefficient P_{I}.

To find γ vs. n and P_{I} vs. n, we first consider the case of initial ATP concentration $C_0 = 8$ mM and solve the 1D Fick's law equation with the same boundary and initial conditions (Eqs. 1-3) for $C(x, t)$. Then we convert ATP concentration $C(x, t)$ to flow speed $\bar{v}(x, t)$ using our power-lawed Michaelis-Menten equation (Supplementary Equation 3), which shows that increasing power law exponents n leads to a slower progression of the active-inactive interface (Supplementary Figure 3b). However, such an n-induced variation in interface progression appears not to interfere with the relation of interface displacement with time; we find that the squared interface displacement increases linearly with time across our explored power-law exponents ($n = 0.5$-10; Supplementary Figure 3c), which suggests that interface progression exponent γ will equal 1 regardless of the value of the power-law exponent n in our explored range of exponents (Supplementary Figure 3d inset). Contrarily, we find that the interface progression coefficient decreases with increasing power-law exponents (Supplementary Figure 3d). Overall, our exploration reveals that the active-inactive interface progression exponent being 1 is a consequence of the diffusion-like process of ATP dispersion. This result is insensitive to the choice of flow speed-ATP model (Supplementary Equation 3), but the interface progression coefficient varies rapidly with the model choice. Increasing the power-law exponent from 0.5 to 10 decreases the interface progression coefficient from 740 to 34 μm²/s. Given that our experimentally measured interface progression coefficient $P_{\mathrm{I}} = 451 \pm 8$ μm²/s for 8 mM caged ATP concentration (Fig. 3d), this also suggests that selecting $n = 1$ (or slightly larger than 1) will best match our model with the experimental results (Supplementary Figure 3d) and that Michaelis-Menten kinetics (Eq. 4) is a good approximation to connect ATP concentrations with the local flow speed of active fluid.

The calculations in our Fick's law-based model reveals that the interface progression coefficient for a given C_0 depends on the selected flow speed-ATP relation (Supplementary Figure 3a), which implies that the
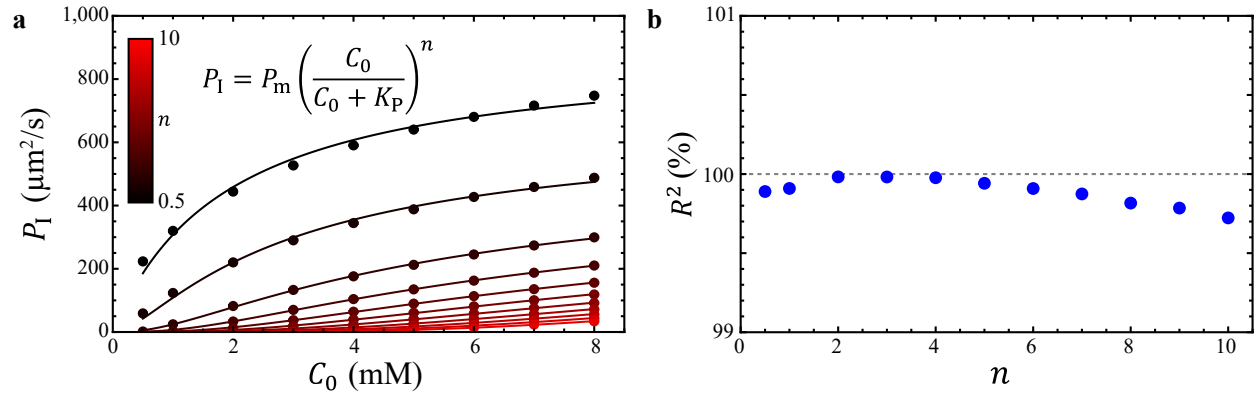
ATP dependence of the interface progression coefficient $P_I(C_0)$ should change with the selected flow speed-ATP relation as well. To investigate, we repeat the above calculation and determine the interface progression coefficients, P_I, as a function of initial ATP concentration, C_0, for power-law exponents n ranging from 0.5 to 10 (dots in Supplementary Figure 4a). Our analysis reveals that increasing the power-law exponents decreases P_I as a function of C_0 (Supplementary Figure 4a) in a similar way that it does for flow speed (Supplementary Figure 3a). Inspired by this observation, we fit each P_I vs. C_0 to their corresponding power-lawed Michaelis-Menten equation with the same power-law exponent n:

$$P_I = P_m \left(\frac{C_0}{C_0 + K_P}\right)^n, \qquad\qquad 4$$

with P_m and K_P as fitting parameters (curves in Supplementary Figure 4a). The resulting data fit well to the equations, with overall goodness of fit $R^2 \geq 0.99$ (Supplementary Figure 4b). This suggests that the ATP dependence in the flow speed can pass to the resulting interface progression coefficient P_I. This analysis also shows that the consistency between the model $P_I(C_0)$ and experimentally measured P_I vs. C_0 (Fig. 3d) is under the condition of $n \approx 1$, which reinforces our assertion that adopting the Michaelis-Menten equation to convert ATP concentration to active fluid flow speed is an appropriate approach for building a coarse-grained model that matches the experimental results.
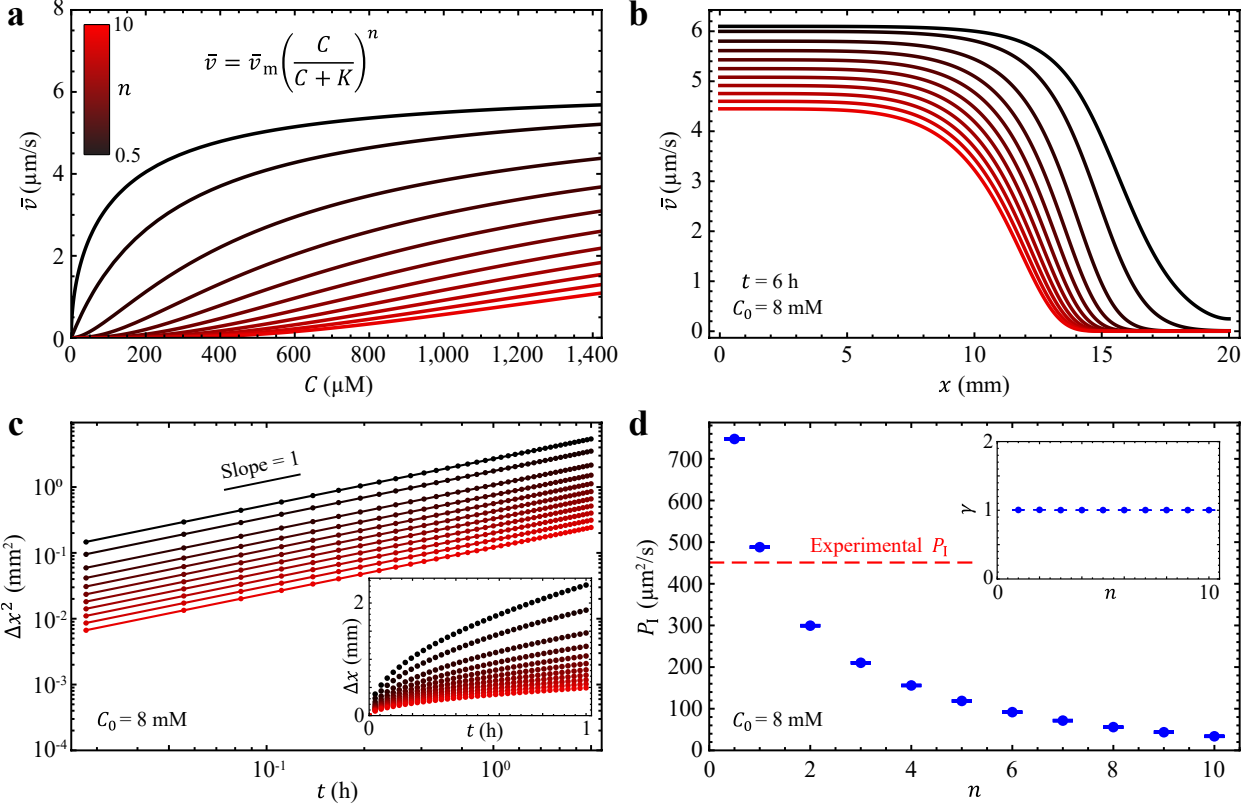
Supplementary Figure 3: (Modeling results) Exploration of the Fick's law-based model with various flow speed-ATP relations. The Fick's law-based model shows that the power-law exponent, n, in flow speed-ATP relation $\bar{v} = \bar{v}_m\{[ATP]/([ATP] + K)\}^n$, influences the interface progression coefficients but not the interface progression exponents. (a) Plot of flow speed of active fluid as a function of ATP concentration, $\bar{v} = \bar{v}_m\{[ATP]/([ATP] + K)\}^n$, with different power-law exponents n, where $\bar{v}_m = 6.2$ μm/s and $K = 270$ μM.[13] (b) The distribution of flow speed at time $t = 6$ hours in the active fluid system for different power-law exponents. Each system has an initial ATP concentration of $C_0 = 8$ mM. The curves are colored based on the n color bar in Panel a. (c) The corresponding squared interface displacement, Δx^2, increases linearly with time, t, for each explored power-law exponent n. The curves are the fitting of $\log(\Delta x^2) = \log(2P_I) + \gamma \log t$ with the interface progression coefficient, P_I, and interface progression exponent, γ, as fitting parameters. Inset: The corresponding interface displacement as a function of time for different power-law exponents. The dots and curves are colored based on the n color bar in Panel a. (d) The corresponding interface progression coefficient, P_I, decreases with power-law exponent n. The red dashed line represents the experimentally measured $P_I = 451 \pm 8$ μm^2/s for 8 mM caged ATP concentration (Fig. 3d). The error bars represent the fitting error in Panel c. Inset: The interface progression exponents remain 1 across explored power-law exponents $n = 0.5$–10. The error bars represent the fitting error in Panel c.

7

Supplementary Figure 4: (Modeling results) The ATP dependence of interface progression coefficient $P_I(C_0)$ is inherent from the ATP dependence of the corresponding flow speed of active fluid $\overline{v}(C)$. (a) Interface progression coefficient, P_I, as a function of initial ATP concentration, C_0, for different power-law exponents n. The curves are the fitting to $P_I = P_m\{[\text{ATP}]/([\text{ATP}] + K_P)\}^n$ with P_m and K_P as fitting parameters. (b) The goodness of fit, R^2, for power-law exponent data in Panel a.

Supplementary Note 3: Analytical expressions for active-inactive interface progression

Our simple Fick's law-based model shows that the diffusion-like progression of the active-inactive interface is the consequence of diffusive dispersion of ATP (Fig. 3c). This result is based on numerical solutions of the Fick's law equation (Eq. 1); to gain deeper insight into the algebra underlying this modeling result, we consider the dynamics far from the boundary (i.e., discarding Eq. 2). The analytical solution to Fick's law (Eq. 1) subject to an initial step distribution is

$$C(x,t) = \frac{C_0}{2} \operatorname{erfc}\left(\frac{x - x_0}{2\sqrt{D\,t}}\right),$$

5

where x_0 is the initial location of the step. We find the rate of progression of the interface by plugging Supplementary Equation 5 into Eq. 4 and solving for the active-inactive interface displacement Δx. Then the squared interface displacement can be written as:

$$\Delta x^2 = 4\,D\,t\,\left[\operatorname{erfc}^{-1}\left(\frac{2K}{C_0 + 2K}\right)\right]^2 = 2P_\mathrm{I}\,t,$$

6

where erfc^{-1} is the inverse of the complementary error function and the interface progression coefficient, P_I, is defined as

$$P_\mathrm{I} \equiv 2D\,\left[\operatorname{erfc}^{-1}\left(\frac{2K}{C_0 + 2K}\right)\right]^2.$$

7

Here, we find that, despite the nonlinearity of the flow speed-ATP conversion (Eq. 4), the interface progression coefficient depends linearly on the diffusion coefficient ($P_\mathrm{I} \propto D$; Supplementary Equation 7) and the progression of the interface remains diffusion-like ($\Delta x^2 \propto t$; Supplementary Equation 6), which is consistent with our numerical results ($\gamma = 1$; Fig. 3c). Moreover, the derived interface progression coefficient $P_\mathrm{I}(C_0)$ is almost identical to the numerical results (magenta curve and red dots in Fig. 3d). We thus reproduce the modeling results (γ and P_I) algebraically.

Supplementary Note 4: Effect of sample container height on the correlation lengths and times of flow velocities

To characterize whether the mixing of our active fluid systems is driven by diffusion-dominated or convection-dominated active transport, we adopt a dimensionless quantity, the Péclet number: $Pe \equiv \bar{v} l_c / D$, where D is the diffusion coefficient of ATP (Supplementary Note 1), $\bar{v}$ is the flow mean speed of active fluid, and l_c is the correlation length of flow velocity of active fluid.[2,3] Determining Pe requires l_c, and our previous work shows that increasing the sample container height can increase l_c.[14] Thus, we characterize how the correlation lengths and correlation times of active fluid flows depend on the sample container height.

To extract the correlation lengths in our sample, we prepare an active fluid sample with uniform activity, dope the sample with fluorescent tracer particles, and monitor and track these tracers to reveal the flow velocity fields of active fluid in the sample $\mathbf{V}(\mathbf{r}, t)$ as a function of time t (Supplementary Figure 5a). Then we calculate the velocity autocorrelation function,

$$\Psi(\Delta\mathbf{r}, \Delta t) \equiv \int d\mathbf{r}\, dt\, \mathbf{V}(\mathbf{r} + \Delta\mathbf{r}, t + \Delta t) \cdot \mathbf{V}(\mathbf{r} + \Delta\mathbf{r}, t + \Delta t), \qquad 8$$

by deploying the convolution theorem

$$\Psi = \mathcal{F}^{-1}\{\mathcal{F}\{\mathbf{V}\} \cdot \mathcal{F}\{\mathbf{V}\}^*\}, \qquad 9$$

where $\mathcal{F}\{\ \}$ represents the Fourier transform, $\mathcal{F}^{-1}\{\ \}$ represents the inverse Fourier transform, and Θ^* represents the complex conjugate of any variable Θ. Then we normalize the correlation function as

$$\overline{\Psi}(\Delta\mathbf{r}, \Delta t) = \frac{\Psi(\Delta\mathbf{r}, \Delta t)}{\Psi(\mathbf{0}, 0)}, \qquad 10$$

which allows us to determine the normalized same-time velocity autocorrelation function as $\overline{\Psi}(\Delta\mathbf{r}, 0)$ (Supplementary Figure 5b). To analyze the correlation lengths, we average the correlation function over orientations

$$\overline{\Psi}(\Delta r, 0) = \langle \overline{\Psi}(\Delta\mathbf{r}, 0) \rangle_{|\Delta\mathbf{r}|=\Delta r}, \qquad 11$$

where $\langle\ \ \rangle_{|\Delta\mathbf{r}|=\Delta r}$ indicates averaging over the same magnitude of spatial displacement $\Delta\mathbf{r}$ (Supplementary Figure 5c). Then we define the correlation lengths l_c as the separation distance where the normalized correlation function decays to 0.5: $\overline{\Psi}(l_c, 0) \equiv 0.5$. Repeating the analysis of l_c over the samples with heights varying from 60 to 700 μm reveals that the correlation lengths increase from 60 to 210 μm (Supplementary Figure 5d). Given that the correlation lengths also represent the size of vortices in active fluid flow,[15] our analysis suggests that across our explored sample heights the vortices expand by a factor of 3.5.

In addition to correlation lengths, our analysis also allows us to extract the correlation time, τ_c, which reveals how rapidly the flow patterns change (i.e., the lifetime of vortices). To determine the correlation time, τ_c, we follow a similar analysis except we analyze the normalized same-position temporal autocorrelation function $\overline{\Psi}(\mathbf{0}, \Delta t)$ (Supplementary Figure 5c inset) and define the correlation time τ_c as the time lapse when the normalized same-position temporal correlation function decays to 0.5: $\overline{\Psi}(\mathbf{0}, \tau_c) \equiv 0.5$. Our analysis reveals that the correlation time remains ~20 seconds across our explored sample heights (Supplementary Figure 5d inset), which suggests that the sample geometry does not play a significant role in the lifetime of the vortices. Overall, this work shows that increasing the sample container height enlarges

10

the vortices but does not significantly affect their formation and deformation rates, which aligns with our previous studies about length scales of confined active fluid.[14]
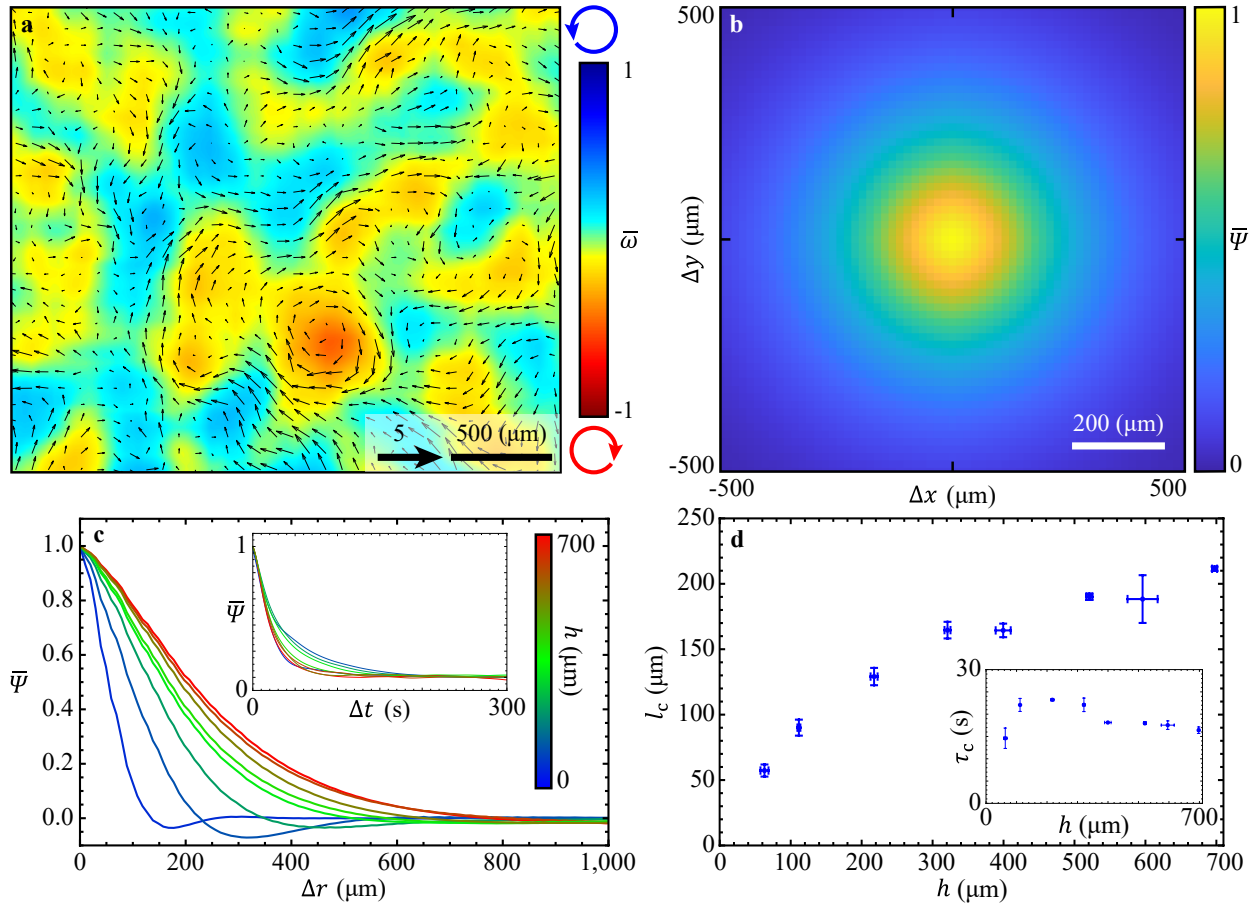
Supplementary Figure 5: (Experimental results) Increasing sample container height increases the correlation lengths of flow velocities but does not significantly influence the correlation times. (a) Normalized velocity field and vorticity color map of active fluid flows in a 700-μm-thick flow cell. The velocity field **V** is normalized by the mean speed of active fluid flow; the vorticity $\omega \equiv [\nabla \times \mathbf{V}]_z$ is normalized by the triple of standard deviation of vorticity, $\overline{\omega} \equiv \omega/[3\,\mathrm{std}(\omega)]$.[16] (b) Map of normalized same-time spatial autocorrelation of flow velocity in the same sample as Panel a. (c) Normalized same-time spatial autocorrelation functions of flow velocity as a function of separation distance (Supplementary Equation 11) for various sample heights. Inset: Normalized same-position temporal autocorrelation functions of flow velocity for various sample heights. (d) The correlation lengths of flow velocity increase with sample height. The error bars represent the standard deviations of two trials. Inset: The correlation times of flow velocity remain nearly invariant (~20 s) for sample heights from 60 to 700 μm.

Supplementary Note 5: Mixing kinematics of activity-uniform active fluid

This work focuses on mixing in active fluid systems with nonuniform distribution of activity. We show that as the Péclet number of a system increases, the progression of the active-inactive interface changes from diffusion-like to superdiffusion-like (Fig. 4b) and the mixing times of suspended fluorescent dyes decrease (Fig. 5c). We decide that it would be elucidating to compare these results with those from active fluid systems with uniform activity distribution. A uniform active fluid system does not have an active-inactive interface, and thus we can not measure γ, but we measure mixing time of suspended fluorescein. We repeat the fluorescein-mixing experiments where the flow speed of active fluid are increased by increasing sample height (Fig. 5), but we perform the experiments in a system with uncaged ATP and thus flow speeds are uniformly distributed throughout the sample (Supplementary Figure 6b inset) and then we analyze the mixing time as a function of mean flow speed and Péclet number (Supplementary Figure 6). Our analysis reveals that the mixing time decreases with increasing Péclet number without a discernible transition, which we expect because a more convective active transport can mix the dye faster. Also, this result is similar to the one in active-inactive fluid systems (Fig. 5c), which suggests that the Péclet number is the controlling parameter for mixing time of suspended components in active fluid systems, regardless of the distribution of activity.
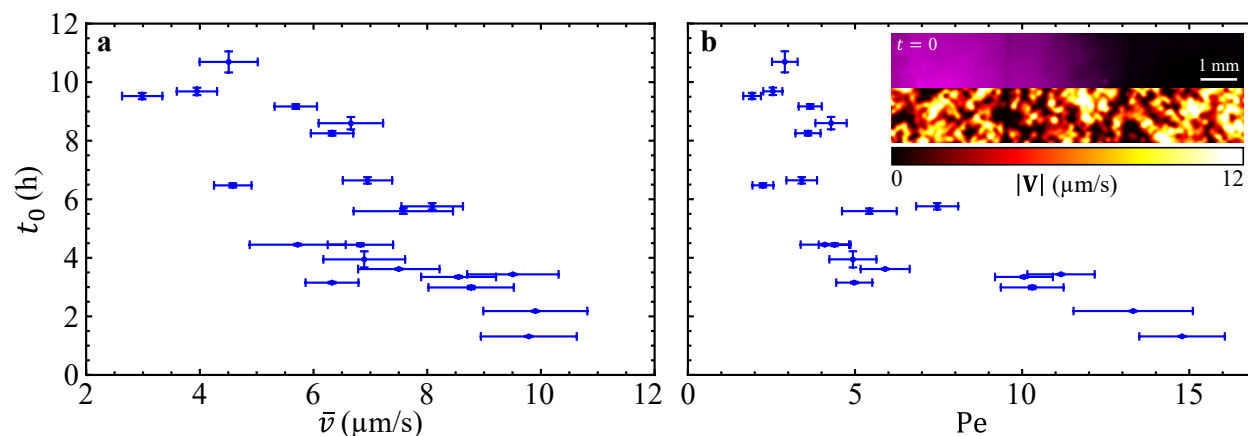
Supplementary Figure 6: (Experimental results) Mixing time of UV-activated fluorescent dyes decreases with increasing Péclet number for activity-uniform active fluid systems. (a) Mixing time as a function of mean speed of active fluid with uniform activity distribution. Accelerating active fluid flows accelerates the mixing process of suspended fluorescein, resulting in shorter mixing time t_0. Each dot represents one experimental measurement. Error bars in t_0 represent the slope fitting error as in Fig. 5b inset, and error bars in $\bar{v}$ represent the standard deviation of time-averaged flow speeds. (b) Mixing time in activity-uniform active fluid systems decreases with increasing Péclet number. The error bars are as in Fig. 5c. Inset: Micrograph of fluorescein uncaged by ultraviolet light exposure (magenta in upper half) and speed map of active fluid (lower half) in the beginning ($t = 0$) of the dye-mixing sample that had mean speed $\bar{v} \approx 9.8 \pm 0.8$ μm/s and mixing time $t_0 = 1.31 \pm 0.02$ h. Note that active fluid has uniform activity (flow speed distribution) in the beginning whereas the uncaged fluorescein is only distributed on one side (left) of the sample.

Supplementary Note 6: Network melting mechanism may slow progression of active-inactive interface

Our active-inactive fluid experiments show that for the active-inactive interface to progress, not only does ATP need to be transported to the inactive fluid region, but also the inactive microtubule network needs to be activated from its inactive state (Supplementary Movie 1). However, inactive microtubule networks behave like an elastic gel because the unfueled kinesin motor dimers are immobile and act as crosslinkers in the microtubule network,[8] and after ATP is transported to the active-inactive interface, it takes time for the fueled motors to fluidize or melt the inactive microtubule network[1] so the interface can progress. Thus, the active-inactive interface is expected to progress more slowly than it would if the network could melt instantly.

To examine this expectation, we analyze the normalized speed profile expected on the basis of ATP distribution and compare them with the measured normalized speed profile. We assume that the ATP is transported by the active fluid in the same way as fluorescein. Also, because ATP and fluorescein are both activated by UV light exposure, we assume that the distribution of dyes is similar to that of activated ATP, which implies that the fluorescein and activated ATP has similar concentration profiles: $C_{\mathrm{ATP}}(x,t)/C_{\mathrm{ATP0}} \approx C_{\mathrm{fluorescein}}(x,t)/C_{\mathrm{fluorescein0}}$ where $C_{\mathrm{X}}(x,t)$ represents the concentration of X and C_{X0} represents the initial concentration of X. We also assume that the gray values in the fluorescein micrographs are proportional to uncaged fluorescein concentration, which implies that the normalized concentration profile of uncaged fluorescein is similar to the normalized profile of gray values (G.V.) in the fluorescein micrographs: $C_{\mathrm{fluorescein}}(x,t)/C_{\mathrm{fluorescein0}} \approx \overline{\mathrm{G.V.}}(x,t)$. Thus, we can deduce the profile of ATP from normalized profile of gray values in fluorescein micrographs: $C_{\mathrm{ATP}}(x,t) \approx C_{\mathrm{ATP0}}\,\overline{\mathrm{G.V.}}(x,t)$. To extract the normalized profile of gray values in fluorescein micrographs, we consider the micrographs of fluorescein near the active-inactive interface (Supplementary Figure 7a). Then we average the gray values of a micrograph vertically to get a profile of gray values, G.V.(x,t) (Supplementary Figure 7c). To normalize the gray value profile, we adopt the baseline model, which introduces two baselines as the upper and lower references of the gray values: $L_{\mathrm{U}}(x,t)$ and $L_{\mathrm{L}}(x,t)$, where L_{U} is determined by fitting the gray value profile in the active bulk to a line (Supplementary Fig. 6c, magenta curve on top left) and L_{L} is determined by fitting the gray value profile in the inactive bulk to a line (Supplementary Figure 7c, magenta curve on bottom right). Then, the gray value profile can be normalized as

$$\overline{\mathrm{G.V.}}(x,t) \equiv \frac{\mathrm{G.V.}(x,t) - L_{\mathrm{U}}(x,t)}{L_{\mathrm{U}}(x,t) - L_{\mathrm{L}}(x,t)}. \qquad 12$$

This normalization model has been commonly used in the analysis of thermal melting curves of DNA.[17] Here, we adopt this normalization model to reduce the influences of background light and nonuniform illumination in our profile analysis. Once the normalized gray value profile is determined, we can deduce the profile of ATP concentrations (Supplementary Figure 7d). Then we convert the ATP concentration profile to flow speed profile of active fluid with the Michaelis-Menten equation (Eq. 4) followed by normalizing the flow speed profile (blue curve in Supplementary Figure 7e). This is the profile deduced from distribution of uncaged fluorescein. To compare the deduced speed profile with the directly measured speed profile, we analyze the tracer motion at the same time to extract the speed distribution of active fluid flow (Supplementary Figure 7b), average the speed distribution vertically to extract the speed profile, and normalize the profile (red curve in Supplementary Figure 7e). Our analysis shows that the normalized speed profile extracted from tracer motion (red curve in Supplementary Figure 7e) falls behind the profile deduced from uncaged fluorescein distribution (blue curve), which demonstrates that the active-inactive interface progresses more slowly than expected from ATP distribution, and that the network melting plays a role in the progression of the active-inactive interface and can slow down the progression.

The network melting mechanism is absent in our active-fluid hydrodynamic model; the model assumes that the network can melt almost instantly upon arrival of ATP (with negligible warm-up time from the initial development of activity-driven instability in the extensile $\mathbf{Q}$ field[1,18]), so we expect that the profile discrepancies observed in the experiment (Supplementary Figure 7e) will not exist in our model. To examine the validity of our expectation, we analyze the profiles both directly from flow speed distribution and as calculated on the basis of ATP distribution. In the simulation, we can directly access the ATP distribution (Supplementary Figure 8a), which allows us to determine the corresponding ATP concentration profile (Supplementary Figure 8c inset). Then we convert the concentration profile to speed profile by the Michaelis-Menten equation (Eq. 4) followed by normalization to extract the normalized speed profile (blue curve in Supplementary Figure 8c). To compare this ATP-based profile with the profile from flow speed distribution, we consider the speed map at the same time (Supplementary Figure 8b), average the speed distribution vertically to get the speed profile, and normalize the profile to get the normalized speed profile (red curve in Supplementary Figure 8c). The modeling results show that the ATP-based speed profile and the flow speed-based speed profile nearly overlap across the active-inactive interface, which means that, in the simulation, ATP and activity progress at the same pace. This is not consistent with experimental observations that the progression of activity falls behind ATP (Supplementary Figure 7e). This mismatch between experiments and model results support the existence of a network melting mechanism—in which the network needs to undergo a melting process before it can become fluidized—which is absent in the model.

14
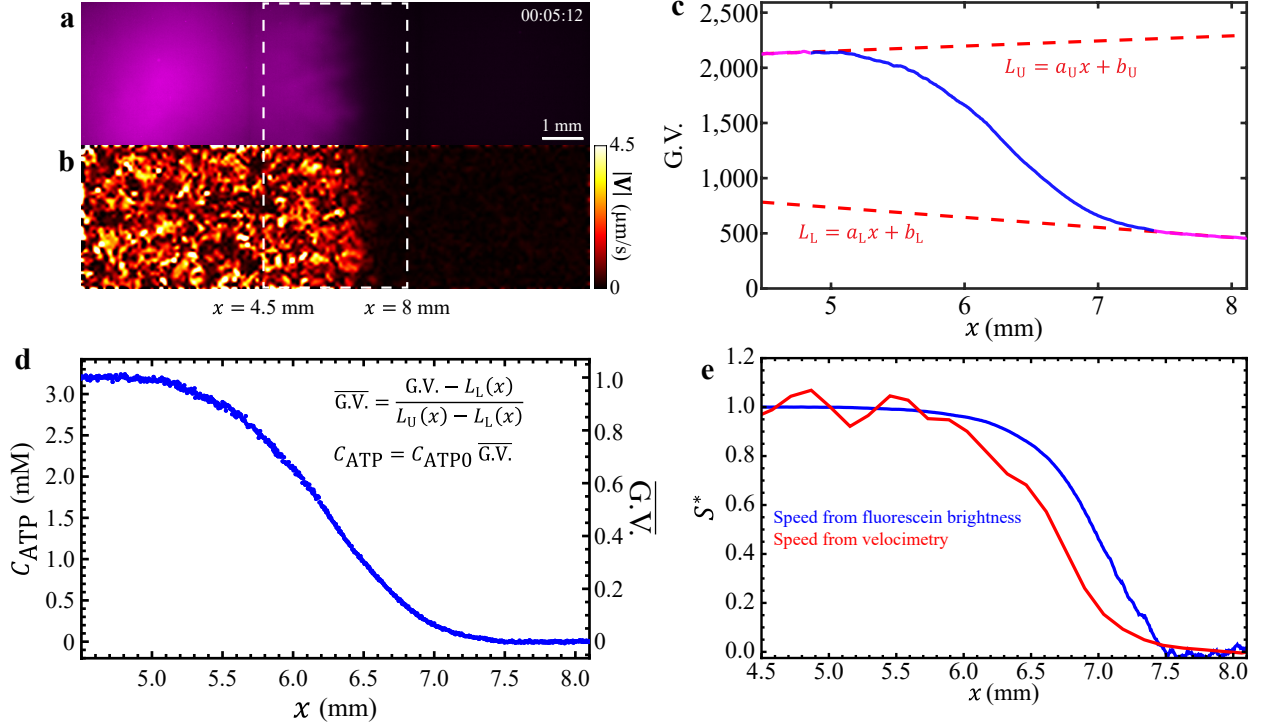
Supplementary Figure 7: (Experimental results) The active-inactive interface progresses more slowly than expected from distribution of ATP. (a) Micrograph of fluorescein (magenta) in the active-inactive sample with an initial ATP concentration of $C_{ATP0} = 3.2$ mM. The fluorescein is initially caged and thus does not fluoresce; exposure of the left side of the sample to ultraviolet light both activate the microtubule-kinesin fluid and uncaged the fluorescein, allowing it to fluoresce. The white dashed rectangle is the region of interest in the analysis in Panels c-e. The time stamp represents hour:minute:second. (b) The corresponding map of flow speed of active fluid deduced from tracking the motion of tracers. (c) Profile of gray values of the fluorescein micrograph in Panel a. The profile is normalized with a baseline model[17] that includes an upper baseline determined by a line fitting to the gray value profile in the active bulk (the top-left magenta portion of the profile), $L_U = a_U + b_U$ where $a_U = 46$ mm^{-1} and $b_U = 1,920$, and a lower baseline determined by a line fitting to the gray value profile in the inactive bulk (the bottom-right magenta portion of the profile), $L_L = a_L + b_L$ where $a_L = -91$ mm^{-1} and $b_L = 1,190$. These two baselines serve as the upper and lower references for profile normalization. (d) The gray values are normalized by the baseline model (right axis). The profile of ATP concentrations is deduced by scaling the normalized profile of gray values by the initial concentrations of ATP, C_{ATP0} (left axis). (e) The profile of ATP concentrations is converted to the profile of flow speed by the Michaelis-Menten equation (Eq. 4). The speed profile is normalized (blue curve) as in Fig. 1e and the normalized profile is then compared with the profile measured from the velocimetry of tracers (red curve). The profile analyzed from the velocimetry falls behind the profile deduced from fluorescein brightness, which suggests that the melting mechanism of the crosslinked microtubule network slows the progression of the active-inactive interface.
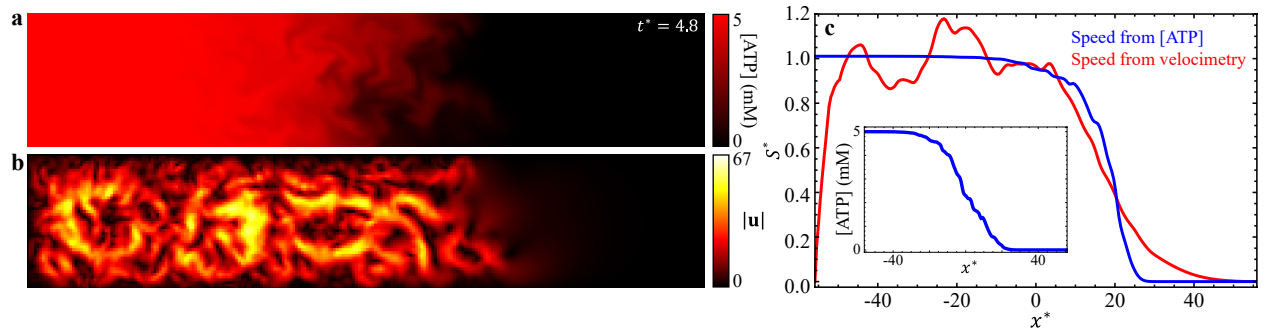
Supplementary Figure 8: (Modeling results) Simulated profiles of active fluid flow and profiles deduced from simulated ATP concentration distribution overlap. (a) Distribution of ATP concentrations in the active fluid simulation (Fig. 6) with $\alpha_0^* = 25$ and $D^* = 2$ at $t^* = 4.8$. (b) The corresponding distribution of flow speed. Note that the flow speed quickly drops to zero (black) as it approaches the boundaries because of the no-slip boundary condition. (c) The corresponding normalized speed profile analyzed from the distribution of flow speed (red curve) and the normalized speed profile deduced from the distribution of ATP (blue curve) nearly overlap at the active-inactive interface. This suggests that, in the simulation, the active fluid is activated almost immediately after the ATP is transported to its location. Inset: The profile of ATP concentrations in Panel a, averaged vertically.
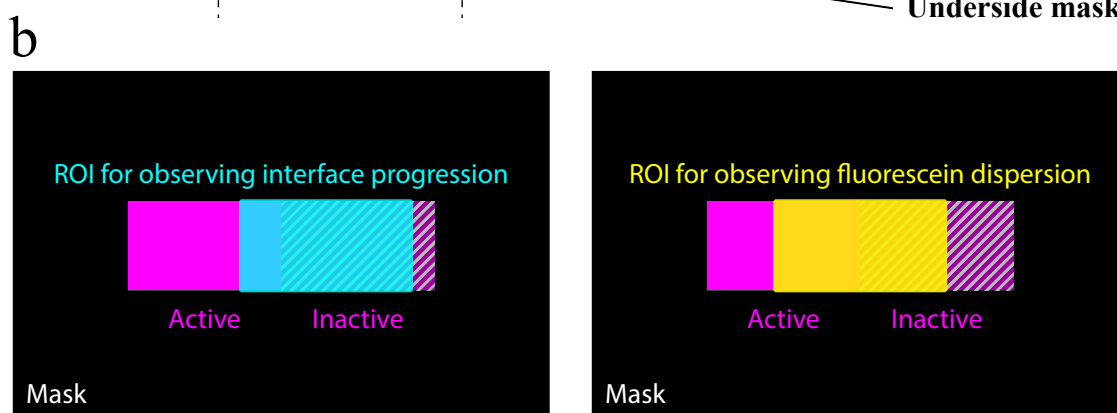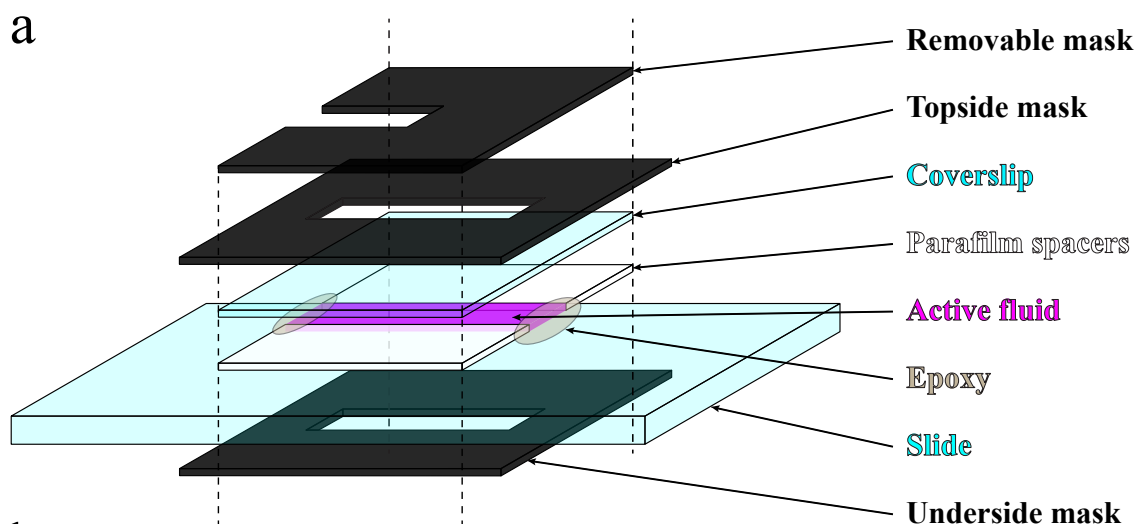
Supplementary Figure 9: Removable masks are used to activate one side of the sample. (a) Active fluid is loaded into a glass flow cell consisting of a polyacrylamide-coated glass slide and coverslip with Parafilm as a spacer and sealed with epoxy. To prepare the active-inactive fluid system, we block one side of the sample (right half) with a removable mask. To prevent UV light from being scattered to the masked region by the epoxy and Parafilm, which can cause unwanted fluid activation in the masked region, we further block the rest of the sample, including epoxy and Parafilm, with 2 masks (one topside and one underside). After the UV exposure, we remove the masks to image the sample with fluorescent microscopy. (b) The sample is 20 mm long, which is wider than the field of view in our microscope even using a 4× objective, so we image 3 to 4 adjacent frames along the flow cell and stitch these frames into one large image. For the experiments monitoring active-inactive fluid interface progression (left), we select the region of interest (ROI) as one quarter of active area and most of the inactive area (cyan rectangle) to observe the progression of the interface (Figs. 1–4). For the experiments monitoring the dispersion of fluorescein (right), we select the ROI as half of the active and half of the inactive regions (yellow rectangle) to observe how one-sided dyes disperse to the rest of the sample (Fig. 5).

Assembled slide with removable mask
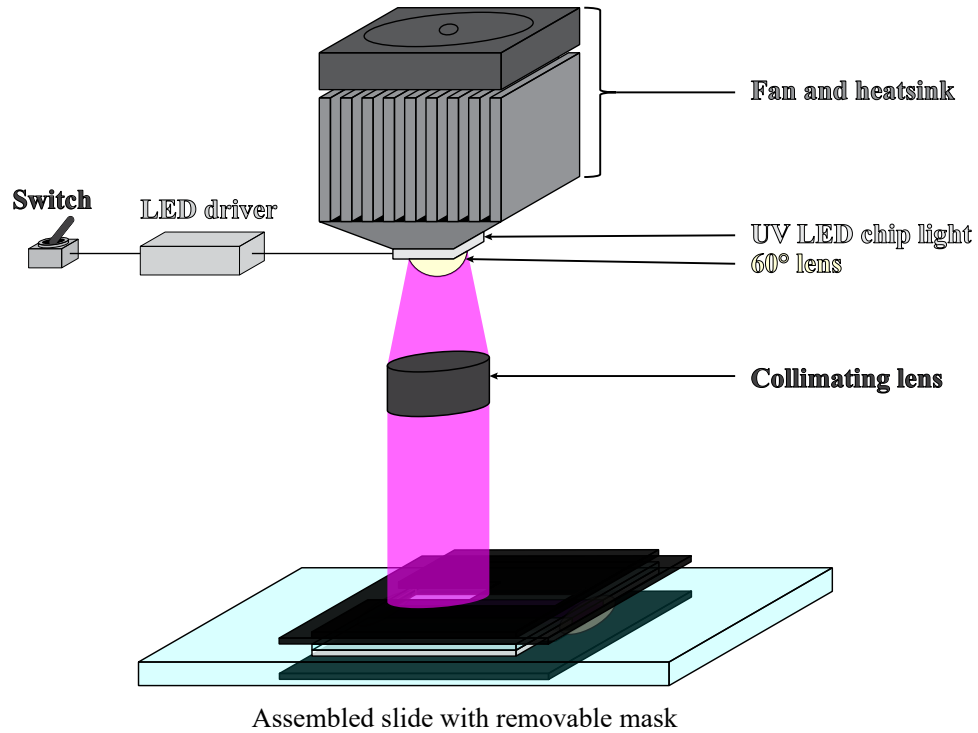
Supplementary Figure 10: Setup to apply UV light to the masked sample.[19] UV light is emitted with a UV LED chip (Amazon, B01DBZK2LM) powered by an LED driver (McMaster, 4305N124) and cooled with a fan-powered heatsink (Amazon, B01D1LD68C). To ensure that the light exposure was consistent across the sample, we parallelize the emitted UV light beams with a 60° lens (part of the heatsink) and a collimating lens (part of the microscope, Nikon, MEA54000).

Supplementary Movie 1: (Experimental results) Mixing of activated and inactive fluids. The fluid contains caged ATP, which can not fuel the kinesin motors until it is uncaged by exposure to ultraviolet light. After one side of the sample is exposed to ultraviolet light, the ATP molecules on that side of the sample are released and can fuel the kinesin motors to drive microtubules and create flows. The activated fluid blends with the inactive fluid until two fluids become one activity-uniform fluid. Cyan fibers are microtubules and red dots are tracers. The time stamp indicates hour:minute:second.

Supplementary Movie 2: (Modeling results) Results of a one-dimensional Fick's law-based model that simulates the mixing of active and inactive fluid under low Péclet number conditions (Pe $\lesssim$ 3). The model describes how ATP distribution evolves from one side of a container to being uniformly distributed (top). The ATP is confined in a segment from $x = 0$ to $x = 20$ mm. The ATP distribution is converted to distribution of active fluid mean speed via Michaelis-Menten kinetics (Fig. 3b). The simulation shows that initially only one side of the system is activated, and then the system evolves toward an activity-uniform state (bottom). Active fluid with a higher initial concentration of ATP (8 mM; red curve) evolves toward an activity-uniform state faster than active fluid with a lower initial concentration of ATP (1 mM; black curve). The time stamp indicates hour:minute:second.

Supplementary Movie 3: (Experimental results) Dispersion of UV-activated fluorescent dyes suspended in inactive (top) and active (bottom) microtubule-kinesin fluid. In the inactive system, the dyes are dispersed only by molecular diffusion, whereas in the active fluid system, the dyes are further transported by active fluid flows and thus disperse through the sample more quickly. Time stamp indicates hour:minute:second.

Supplementary Movie 4: (Modeling results) Simulated maps of ATP concentrations and flow speeds of active fluid for various pairs of dimensionless activity level α_0^* and dimensionless molecular diffusion coefficient D^*. In the no-activity system ($\alpha_0^* = 0$; top), dispersion of ATP is driven only by molecular diffusion ($D^* = 16$). When the fluid is activated ($\alpha_0^* = 25$; middle), the chaotic turbulence-like mixing flows are developed to actively transport ATP, which speeds up the ATP dispersion. When the ATP diffusivity is increased ($D^* = 64$, bottom), dispersion of ATP is further accelerated. The simulation captures the roles of ATP diffusion and active fluid-induced convection in dispersing ATP.

Supplementary Movie 5: (Experimental results) Mixing of checkerboard-patterned fluorescein and activity. The checkerboard-pattern distribution of fluorescein and activity is achieved by applying UV light (00:00:12–00:01:06) in a checkerboard pattern to inactive fluid with caged ATP and caged fluorescein. The uncaged fluorescein (magenta in the left panel) is actively transported by flows driven by active microtubule network (cyan fibers in the middle panel) with the same checkerboard pattern of activity and reaches a homogeneously-distributed state in 10 minutes (00:10:30). The right panel represents the merged images of fluorescein (left) and microtubules (middle). The grid size of the checkerboard is $a = 1$ mm. The time stamp indicates hour:minute:second.

Supplementary Movie 6: (Modeling results) Simulation of active and inactive fluid systems with initial checkerboard-patterned ATP. Simulated maps of ATP concentrations (top row) and flow speeds of fluids (bottom row) for active (right column) and inactive (left column) fluid systems where ATP is initially distributed in a checkerboard pattern with a dimensionless grid size of $a^* = 22$. The active fluid system ($\alpha_0^* = 25$; left) actively transports and homogenizes ATP within the dimensionless time $t^* = 10$, while the ATP in the inactive fluid system ($\alpha_0^* = 0$; right), which relies on molecular diffusion ($D^* = 1$) to disperse ATP, does not reach the homogeneous state until the dimensionless time $t^* = 80$.

Supplementary References

1   Najma, B. et al. Dual antagonistic role of motor proteins in fluidizing active networks. *arXiv:2112.11364 [cond-mat.soft]*. (2021).

2   Tuval, I. et al. Bacterial swimming and oxygen transport near contact lines. *Proc Natl Acad Sci U S A* **102**, 2277-2282 (2005).

3   Senoussi, A., Galas, J.-C. & Estevez-Torres, A. Programmed mechano-chemical coupling in reaction-diffusion active matter. *Sci Adv* **7**, eabi9865 (2021).

4   Radomsky, M. L., Whaley, K. J., Cone, R. A. & Saltzman, W. M. Macromolecules released from polymers: Diffusion into unstirred fluids. *Biomaterials* **11**, 619-624 (1990).

5   Saltzman, W. M., Radomsky, M. L., Whaley, K. J. & Cone, R. A. Antibody diffusion in human cervical mucus. *Biophys J* **66**, 508-515 (1994).

6   Soeller, C. et al. Application of two-photon flash photolysis to reveal intercellular communication and intracellular Ca2+ movements. *J Biomed Opt* **8**, 418-427 (2003).

7   Casalini, T., Salvalaglio, M., Perale, G., Masi, M. & Cavallotti, C. Diffusion and aggregation of sodium fluorescein in aqueous solutions. *J Phys Chem B* **115**, 12896-12904 (2011).

8   Gagnon, D. A. et al. Shear-induced gelation of self-yielding active networks. *Phys Rev Lett* **125**, 178003 (2020).

9   Bowen, W. J. & Martin, H. L. The diffusion of adenosine triphosphate through aqueous solutions. *Arch Biochem Biophys* **107**, 30-36 (1964).

10 Schnitzer, M. J. & Block, S. M. Kinesin hydrolyses one ATP per 8-nm step. *Nature* **388**, 386-390 (1997).

11 Coy, D. L., Wagenbach, M. & Howard, J. Kinesin takes one 8-nm step for each ATP that it hydrolyzes. *J Biol Chem* **274**, 3667-3671 (1999).

12 Howard, J., Hudspeth, A. J. & Vale, R. D. Movement of microtubules by single kinesin molecules. *Nature* **342**, 154 (1989).

13 Bate, T. E., Jarvis, E. J., Varney, M. E. & Wu, K.-T. Collective dynamics of microtubule-based 3D active fluids from single microtubules. *Soft Matter* **15**, 5006-5016 (2019).

14 Fan, Y., Wu, K.-T., Aghvami, S. A., Fraden, S. & Breuer, K. S. Effects of confinement on the dynamics and correlation scales in kinesin-microtubule active fluids. *Phys Rev E* **104**, 034601 (2021).

15 Varghese, M., Baskaran, A., Hagan, M. F. & Baskaran, A. Confinement-induced self-pumping in 3D active fluids. *Phys Rev Lett* **125**, 268003 (2020).

16 Wu, K.-T. et al. Transition from turbulent to coherent flows in confined three-dimensional active fluids. *Science* **355**, eaal1979 (2017).

17 Mergny, J.-L. & Lacroix, L. Analysis of thermal melting curves. *Oligonucleotides* **13**, 515-537 (2003).

18 Saintillan, D. & Shelley, M. J. Instabilities, pattern formation, and mixing in active suspensions. *Phys Fluids* **20**, 123304 (2008).

19 Berezney, J., Goode, B. L., Fraden, S. & Dogic, Z. Extensile to contractile transition in active microtubule-actin composites generates layered asters with programmable lifetimes. *Proc Natl Acad Sci U S A* **119**, e2115895119 (2022).